Environmental Fluid Mechanics (2022) 22:971–1003
https://doi.org/10.1007/s10652-022-09875-0

ORIGINAL ARTICLE

Shallow fluid flow over an obstacle: higher-order non-hydrostatic modeling and breaking waves

Oscar Castro-Orgaz[1] · Francisco N. Cantero-Chinchilla[1] · Hubert Chanson[2]

Received: 28 March 2022 / Accepted: 18 May 2022 / Published online: 10 June 2022

Abstract

The simulation of shallow flows over obstacles is an important problem in environmental fluid dynamics, including exchange flows over seabed sills, atmospheric flows past steep mountains and water flows over river bedforms. A common mathematical treatment consists in using vertically-averaged models instead of vertically-resolved ones by introducing a suitable shallow water approximation. The dispersionless Saint Venant equations are a useful tool, albeit accuracy is not enough in many circumstances. The next approach consists in resorting to the Serre–Green–Naghdi theory, which is well known to produce good solutions for long non-breaking waves. However, a common feature of flows over obstacles is the generation of breaking waves at its lee side, which are important to model, given their role in the mixing and transport of passive scalars downstream of the terrain barrier. The Serre–Green–Naghdi theory fails to model these flows, producing unrealistic trains of undular waves. A widely used practice consist in resorting to a patching approach in a numerical setting where the solutions of Serre–Green–Naghdi and Saint Venant equations are assembled once wave breaking is detected by case-dependent empirical parameters. In this work an alternative method to dealt with wave breaking over obstacles within the Boussinesq-type approximation is proposed. The exact depth-averaged equations for flows over uneven beds are developed and presented as function of the vertical acceleration and non-uniformity of velocity with elevation. By introducing a suitable kinematic field, a new high-order phase resolving system of non-hydrostatic equations is presented, containing the usual dispersive corrections of Serre–Green–Naghdi theory plus high-order corrections for velocity profile modeling. It is found that the new theory allows the simulation of both breaking and non-breaking waves in shallow flows over obstacles without introducing any case-dependent calibration parameter. The new shallow water approximation is thus an alternative method to deal with wave breaking in Boussinesq type models.

Keywords Obstacles · Saint–Venant equations · Serre–Green–Naghdi equations · Shallow water approximations · Surges · Wave breaking

✉ Oscar Castro-Orgaz
ag2caoro@uco.es

Extended author information available on the last page of the article

1 Introduction

The shallow-water flow over obstacles is an important problem in environmental fluid mechanics, as in the river flow over dunes and antidunes, in oceanographic exchange flows over a seamount, or in the mesoscale atmospheric flow past a steep mountain [1, 2]. A common mathematical simplification to study these flows consists in introducing a shallow water approximation after averaging the hydrodynamic equations in the vertical direction. Depending on the underlaying assumptions different degrees of accuracy are possible in a shallow water approximation. If the vertical acceleration and the non-uniformity of velocity with elevation are neglected in the Euler equations, the ensuing shallow water approximation consists in the Saint Venant equations [3–5]. This approximation has been used to investigate flows over obstacles in seminal works [6, 7], and it is a widely used tool [4]. However, the dispersionless representation of the flow reduce considerably the accuracy of solutions [1, 8].

An alternative shallow water approximation is the Serre–Green–Naghdi theory [9–15], which basically produces weakly-dispersive fully-nonlinear Boussinesq equations [16–18]. This theory was derived by Serre [9] assuming that the streamwise velocity component is uniform with elevation, and by Su and Gardner [10] considering that such velocity component varies parabolically, the result of assuming irrotational flow. The conundrum of having the same phase resolving model either assuming that the velocity is equal to its depth-averaged value or that it follows a parabolic irrotational profile lies in the restriction of the depth-averaged model to second order accuracy in terms of a shallowness parameter [1, 2]. High-order terms arising from considering that the velocity profile is parabolic are routinely discarded. Naghdi and Vongsarnpigoon [19] and Zhu and Lawrence [2] applied the steady form of the Serre–Green–Naghdi equations to flows over sills involving a transition from upstream subcritical flow to downstream supercritical flow, e.g., the possibility of having a hydraulic jump at the lee side of the obstacle was excluded. They found accurate solutions of this theory for test cases with significant vertical acceleration in the flow. Nadiga et al. [1] applied the Serre–Green–Naghdi theory to simulate the time-dependent flow adjustment over an obstacle when it is inserted into a stream initially with uniform flow conditions. This has been a traditional test to investigate the non-linear flow adjustment over topography in meteorology and oceanography [6, 7, 20]. Nadiga et al. [1] found that the upstream non-breaking waves were accurately described by the Serre–Green–Naghdi theory, but the undular dispersive waves predicted at the lee side of the obstacle were unrealistic as compared to the breaking waves predicted by the full Euler equations.

Breaking waves at the lee-side of obstacles are important (Fig. 1), as for example in a oceanographic flow of salt water moving over a sill in a fresh water environment [21, 22]. These waves produce mixing between layers, and, therefore, provides nutrients and dissolved oxygen for the deep water. Further, the dispersion of pollutants in a stream, including suspended sediment, will be enhanced by breaking waves. Therefore, a non-hydrostatic shallow-water representation with ability to simulate both undular and broken waves is needed to simulate flow over obstacles. Some recent 3D non-hydrostatic models [23, 24] have been presented to predict shallow water flows over an obstacle.

The Serre–Green–Naghdi theory was found to produce reliable dam break flow solutions for dry bed tailwater conditions [25, 26] as well as for wet conditions if resulting in undular flows [25]. However, it was found that breaking waves were not adequately simulated. Thus, a widely used approach within the Boussinesq-type framework consists

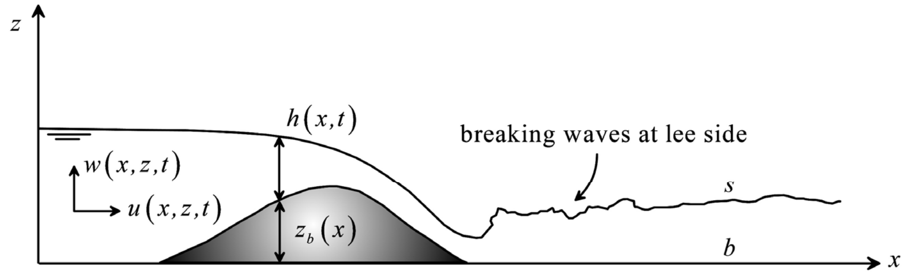

(a) Definition sketch of two-dimensional flow over an obstacle with downstream breaking waves

(b) Saltwater intrusion weir structure in Korea in May 2013 - Top: view from upstream, noting the slots for low flows; Bottom: views from downstream during dry weather (Left) and during a flood event (Right)

Fig. 1 Environmental flows over an obstacle with downstream breaking waves

in using hybrid models combining the Serre–Green–Naghdi and Saint Venant equations [25–28]. The method consists in solving the Serre–Green–Naghdi equations and using some physical sensors, empirically calibrated as the onset of breaking, to detect the breaking portions of the waves in the computational domain. At those portions where breaking is detected, Saint–Venant equations are locally solved and used to produce a solution.

(c) Breaking waves downstream of an overshot vertical gate, used to prevent saltwater intrusion in April 2004 (Dahouët, France)

Fig. 1 (continued)

Basically, it amounts to assume that dissipation at breaking waves is adequately quantified in a depth-averaged sense by the shocks produced by the Saint Venant equations. The method is quite useful, but some challenging numerical issues arise, as for example instabilities at the patching zones of Serre–Green–Naghdi and Saint Venant equations during a mesh refinement [29].

Castro-Orgaz and Chanson [25] reconsidered the wave breaking problem in Boussinesq equations with application to the dam break wave, and found similar restrictions as Kazolea and Ricchiuto [29], in addition of some misprediction of the surge celerity. Therefore, an alternative method of analysis was initiated based on the work of Su and Gardner [10]. Their work is usually linked in the literature only to the development of Serre–Green–Naghdi theory for irrotational flows over horizontal beds. Su and Gardner [10] development was wider, albeit quite ignored. They presented a general method to produce depth-averaged non-hydrostatic equations, where the role of the vertical acceleration and non-uniform velocity with elevation was directly accounted for. Su and Gardner [10] development is limited to horizontal beds, but they explicitly stated the high-order corrections needed to account for the differential advection of momentum originating from the parabolic velocity profile in Serre–Green–Naghdi models. In other words, they stated how to get high-order Serre–Green–Naghdi models accounting for the variation of velocity profile with elevation, although their final equation was the standard streamwise momentum equation of Serre–Green–Naghdi theory. Castro-Orgaz and Chanson [25] considered the full development of Su and Gardner [10] and numerically solved the high-order equations resulting for the case of dam break waves over horizontal terrain. They found that at breaking waves the high-order corrections were of an order of magnitude comparable to that of the standard dispersive term modeled in the Serre–Green–Naghdi theory. The consequence of solving this high-order model was the mimicking of wave breaking automatically by producing shocks in the solution. These shocks were the result of a balance between the dispersive term of the standard Serre–Green–Naghdi theory and the high-order contributions originating from variation with elevation of the velocity profile.

The high-order equations by Su and Gardner [10] were found to be a feasible alternative to deal with wave breaking within the Boussinesq-type framework [25], but only dam break waves over horizontal beds were so far analyzed. As previously discussed, flows over topography are of general interest in environmental fluid flow modeling, and breaking waves are important in flows over obstacles. Therefore, in this work, the Su and Gardner [10] development is generalized for flows over uneven bathymetry, thereby resulting the exact depth-averaged equations. Assuming a velocity field identical to that used in the Serre–Green–Naghdi theory, a new high-order system of equations is derived and applied to the case of shallow flows over obstacles with breaking waves. Results of this new shallow water approximation for flows over topography are systematically compared to Serre–Green–Naghdi and Saint Venant theories, showing the increased accuracy of the former. Given that we found stability problems with hybrid models combining the Serre–Green–Naghdi and Saint Venant equations, these models were not further considered in this research.

2 Vertically-averaged hydrodynamic equations

2.1 Derivation

The purpose of this section is to present a general procedure to generate depth-averaged non-hydrostatic evolution equations for flows over uneven beds following Su and Gardner [10]. They limited their development to water waves over horizontal terrain, so we start here by generalizing the procedure for uneven bathymetry. The Euler equations for flows over a fixed uneven topography (Fig. 1) are as follows [30–32]:

$$\frac{\partial u}{\partial x} + \frac{\partial w}{\partial z} = 0, \tag{1}$$

$$\frac{Du}{Dt} = \frac{\partial u}{\partial t} + u\frac{\partial u}{\partial x} + w\frac{\partial u}{\partial z} = -\frac{1}{\rho}\frac{\partial p}{\partial x}, \tag{2}$$

$$\frac{Dw}{Dt} = \frac{\partial w}{\partial t} + u\frac{\partial w}{\partial x} + w\frac{\partial w}{\partial z} = -g - \frac{1}{\rho}\frac{\partial p}{\partial z}. \tag{3}$$

Here u and w are the velocity components in the x-horizontal and z-vertical directions, respectively; p is the fluid pressure; g is the gravity acceleration; ρ is the water density; and t is time. Equation (1) is the continuity equation, and Eqs. (2) and (3) are the momentum equations in the x- and z-directions, respectively. $D()/Dt$ stands for the material derivative.

The kinematic boundary conditions at the free surface (subscript s) and bed (subscript b), stating no flow across them, are

$$w_s = \frac{\partial h}{\partial t} + u_s\frac{\partial z_s}{\partial x}, \tag{4}$$

and

$$w_b = u_b\frac{\partial z_b}{\partial x}, \tag{5}$$

where $h(x, t)$ is the water depth and $z_b(x)$ the bed profile.

The free surface dynamic boundary condition states that pressure is constant and equal to zero

$$p_s = 0. \tag{6}$$

Vertically-integrating Eq. (1), applying Leibnitz's rule and setting Eqs. (4) and (5) produces the depth-averaged mass conservation equation [5, 32]

$$\frac{\partial h}{\partial t} + \frac{\partial}{\partial x}(Uh) = 0, \tag{7}$$

where $U(x, t)$ is the depth-averaged x-velocity component. Integration of Eq. (2) from the bed to the free surface and imposing Eqs. (4), (5) and (6) produces the depth-averaged x-momentum balance as follows [32]

$$\begin{gathered}\frac{\partial}{\partial t}(Uh) + \frac{\partial M}{\partial x} = -\frac{p_b}{\rho}\frac{\partial z_b}{\partial x},\\ M = \int\limits_{z_b}^{z_s}\left(u^2 + \frac{p}{\rho}\right)\mathrm{d}z,\end{gathered} \tag{8}$$

where p_b is the bottom pressure and M is the momentum function. Now, the z-momentum balance Eq. (3) is integrated from the bottom to the free surface, resulting the following closure equation for p_b, once $p_s = 0$ is settled,

$$\frac{p_b}{\rho} = gh + h\int\limits_0^1 \frac{Dw}{Dt}\mathrm{d}\eta, \tag{9}$$

where $\eta = (z - z_b)/h$. Next, the integrated pressure at a cross section in M needs to be evaluated as function of the kinematic field. Following Su and Gardner [10] the first moment of Eq. (3) around the bed level is formed by multiplying it by $(z - z_b)$. Straightforward integration by parts produces the desired mathematical statement as follows

$$\int\limits_{z_b}^{z_s} \frac{p}{\rho}\mathrm{d}z = \frac{1}{2}gh^2 + h^2\int\limits_0^1 \eta\frac{Dw}{Dt}\mathrm{d}\eta. \tag{10}$$

Equation (10) permits to rewrite M as function of the velocity $u(x, z, t)$ and vertical acceleration $\mathrm{D}w(x, z, t)/Dt$, that is,

$$M = \int\limits_{z_b}^{z_s}\left(u^2 + \frac{p}{\rho}\right)\mathrm{d}z = h\int\limits_0^1 u^2\mathrm{d}\eta + \frac{1}{2}gh^2 + h^2\int\limits_0^1 \eta\frac{Dw}{Dt}\mathrm{d}\eta. \tag{11}$$

Inserting Eqs. (9) and (11) into Eq. (8) yields the final result for the depth-averaged momentum balance,

$$\frac{\partial}{\partial t}(Uh)+\frac{\partial}{\partial x}\left(U^2h+\frac{1}{2}gh^2\right)+gh\frac{\partial z_b}{\partial x}=-\frac{\partial}{\partial x}\left[h\int_0^1\left(u^2-U^2\right)\mathrm{d}\eta+h^2\int_0^1\eta\frac{Dw}{Dt}\mathrm{d}\eta\right]-\frac{\partial z_b}{\partial x}h\int_0^1\frac{Dw}{Dt}\mathrm{d}\eta. \tag{12}$$

Note that Eq. (12) is an exact depth-averaged equation. It is a generalisation to uneven beds of Su and Gardner's [10] depth-averaged equation. The left hand side of Eq. (12) is simply the dispersionless hyperbolic x-momentum equation of the Saint Venant equations [4]. The terms in the right hand side of Eq. (12) are corrections to account for the non-uniform velocity u and vertical acceleration of the flow.

Now Eq. (12) will be further manipulated to depict how to produce the Serre–Green–Naghdi equations [10, 13, 14, 33], which is an approximate depth-averaged model obtainable from Eq. (12) assuming $u=U$. For this task, the vertical acceleration is decomposed into a component obtained assuming that the u velocity is approximated by its depth averaged value U, Dw_U/Dt, plus a deviation provoked by the non-uniform distribution of u with elevation, namely,

$$\frac{Dw}{Dt}=\frac{\partial w}{\partial t}+u\frac{\partial w}{\partial x}+w\frac{\partial w}{\partial z}=\frac{\partial w}{\partial t}+U\frac{\partial w}{\partial x}+w\frac{\partial w}{\partial z}+(u-U)\frac{\partial w}{\partial x}=\frac{Dw_U}{Dt}+(u-U)\frac{\partial w}{\partial x}. \tag{13}$$

Using Eq. (13) the correction term in the RHS of Eq. (12) is rewritten as follows

$$\begin{aligned}&-\frac{\partial}{\partial x}\left[h\int_0^1\left(u^2-U^2\right)\mathrm{d}\eta+h^2\int_0^1\eta\frac{Dw}{Dt}\mathrm{d}\eta\right]-\frac{\partial z_b}{\partial x}h\int_0^1\frac{Dw}{Dt}\mathrm{d}\eta\\&=-\frac{\partial}{\partial x}\left[\underbrace{h\int_0^1\left(u^2-U^2\right)\mathrm{d}\eta+h^2\int_0^1\eta(u-U)\frac{\partial w}{\partial x}\mathrm{d}\eta}_{B}+\underbrace{h^2\int_0^1\eta\frac{Dw_U}{Dt}\mathrm{d}\eta}_{D}\right]\\&\quad-\frac{\partial z_b}{\partial x}\underbrace{h\int_0^1\frac{Dw_U}{Dt}\mathrm{d}\eta}_{p_1/\rho}-\frac{\partial z_b}{\partial x}\underbrace{h\int_0^1(u-U)\frac{\partial w}{\partial x}\mathrm{d}\eta}_{p_2/\rho},\end{aligned} \tag{14}$$

which permits to finally write Eq. (12) as

$$\frac{\partial}{\partial t}(Uh)+\frac{\partial}{\partial x}\left(U^2h+\frac{1}{2}gh^2\right)+gh\frac{\partial z_b}{\partial x}=-\frac{\partial}{\partial x}(D+B)-\frac{p_1+p_2}{\rho}\frac{\partial z_b}{\partial x} \tag{15}$$

Equations (7) and (15) are the general depth-averaged equations for flows over uneven beds. As previously, the LHS of Eq. (15) is the Saint Venant x-momentum equation, whereas D, B, p_1 and p_2 are correction terms. Note that D is physically a dispersive term appearing in the integral of the pressure forces at a vertical section; it is based on an estimate of the vertical acceleration using the depth-averaged horizontal velocity. The term B includes the effects of the non-uniformity of the horizontal particle velocity with elevation on the momentum flux and the vertical acceleration.

The terms D and p_1 are determined based on U, whereas the deviation of u from U is accounted for in the terms B and p_2. In the usual derivation of the Serre–Green–Naghdi equations the u velocity component is assumed to equal U [9, 14], thereby resulting $B=p_2=0$. If irrotational flow is assumed, then u is found to vary parabolically with z [34, 35], resulting $B=p_2=0$ only if high-order terms are discarded in the ensuing depth-averaged equations [10, 18, 25]. Therefore, Eq. (15) is an exact equation that permits to recover the Serre–Green–Naghdi theory setting $u=U$, or a higher order phase resolving model by inserting a suitable function to model $u(x, z, t)$. For dam break waves propagating over horizontal terrain involving surge breaking, Castro-Orgaz and Chanson [25] found that D and B are of the same order, thus higher-order equations are relevant.

Vertically-averaged models like those obtainable by making suitable hypothesis on Eq. (15) cannot resolve the details of wave breaking [36], as for example an overturning crest [37], given that the position of the free surface is assumed to be a single-valued function of the coordinate x. In the vertically averaged framework, it is accepted that breaking waves are adequately characterized by representing them as shocks in shallow water models [4, 27–29, 38]. Thus, the Saint Venant (SV) equations are usually considered a reliable mathematical tool in this regard [38]. Castro-Orgaz and Chanson [25] found for dam break waves propagation over horizontal terrain that the higher order term B partially suppressed the dispersive term D at breaking portions of non-hydrostatic waves, such that the shallow water representation at these portions of the wave profile was very close to that given by the SV equations. The ensuing practical tool is that the higher-order terms confer wave breaking mimicking ability to the vertically-averaged non-hydrostatic model, a feature which is well-known to be lacking in Serre–Green–Naghdi models. This will be further investigated with the more general equations for uneven beds presented in the ensuing section, with application to shallow fluid flow over obstacles.

2.2 Approximation to the velocity field and shallow flow theory

To produce a practical x-momentum equation from the exact Eq. (15), an approximation to the (u, w) velocity components shall be adopted. The velocity components assuming irrotational flow are as follows [32, 35]:

$$u(x,z,t) = U + \left(2U_x z_{bx} h + U h z_{bxx}\right)\left(\eta - \frac{1}{2}\right) + \left(\frac{1}{2}U_{xx}h^2\right)\left(\frac{1}{3} - \eta^2\right), \quad \eta = \frac{z - z_b(x)}{h(x,t)} \tag{16}$$

$$w(x,z,t) = U z_{bx} - U_x h \eta. \tag{17}$$

This choice is by no means unique, and other approximations may be adopted. Equations (16)–(17) are the starting point of many Serre–Green–Naghdi type models for shallow flows, thus we consider them here too. Therefore, short wave modeling is excluded from the present work. Inserting Eqs. (16) and (17) into Eq. (14) produces the following results for the various integrals on it

$$D = \left(U_x^2 - UU_{xx} - U_{xt}\right)\frac{1}{3}h^3 + \left(U_t z_{bx} + U^2 z_{bxx} + UU_x z_{bx}\right)\frac{1}{2}h^2, \tag{18}$$

$$B = \left(\frac{1}{5}U_{xx}^2 h^2 + \frac{1}{2}U^2 z_{bxx}^2 + 2\,UU_x z_{bx} z_{bxx} - \frac{5}{8}UU_{xx} z_{bxx} h + 2U_x^2 z_{bx}^2 - \frac{5}{4}U_x U_{xx} z_{bx} h\right)\frac{1}{3}h^3, \tag{19}$$

$$\frac{p_1}{\rho} = \left(U_x^2 - UU_{xx} - U_{xt}\right)\frac{1}{2}h^2 + \left(U_t z_{bx} + U^2 z_{bxx} + UU_x z_{bx}\right)h, \tag{20}$$

$$\frac{p_2}{\rho} = \left(\frac{1}{4}U_{xx}^2 h - \frac{1}{2}z_{bxx} UU_{xx} - z_{bx} U_x U_{xx}\right)\frac{1}{6}h^3. \tag{21}$$

We call the higher-order system of Eqs. (7) and (15) [with closure Eqs. (18)-(21)] the Su-Gardner (SG) equations, in recognition to their pioneering work. If higher-order terms are neglected in the new equations then $B = p_2 = 0$, thereby resulting the Serre–Green–Naghdi equations for uneven beds [13, 14, 39].

A numerical model is needed for the solution of these depth-averaged equations, to be presented below.

2.3 Discussion of higher-order corrections

Before presenting the numerical scheme, it is rather illustrative to consider the corrections to Saint Venant equations for the case of horizontal terrain, that is, for $z_b(x) = 0$. Thus, let us consider how the non-uniform velocity u impact the higher-order corrections. Su and Gardner [10] obtained for the differential advection of momentum the result

$$h\int_0^1 \left(u^2 - U^2\right)\mathrm{d}\eta = \frac{1}{45}U_{xx}^2 h^5, \tag{22}$$

but, however, overlooked the impact of the velocity profile on the vertical acceleration and thus on the dynamic pressure integral, given by

$$h^2\int_0^1 \eta(u - U)\frac{\partial w}{\partial x}\mathrm{d}\eta = \frac{2}{45}U_{xx}^2 h^5. \tag{23}$$

Note that Eq. (23) yields an effect just twice that of Eq. (22). Su and Gardner [10] stated as dispersive contribution to the pressure integral the usual term

$$D = h^2\int_0^1 \eta\left(\frac{\partial w}{\partial t} + U\frac{\partial w}{\partial x} + w\frac{\partial w}{\partial z}\right)\mathrm{d}\eta = \left(U_x^2 - UU_{xx} - U_{xt}\right)\frac{1}{3}h^3. \tag{24}$$

The main point is that summing Eq. (22) and (23) the ensuing term may reach an order of magnitude equal to or even larger than that of Eq. (24) at breaking waves. This was found by numerical experimentation and a scaling analysis based on a shallowness parameter [25]. Physically, the differential advection of momentum plus incremental vertical acceleration due to the non-uniform velocity profile may suppress even totally the dispersive effects modeled in Serre–Green–Naghdi models. In other words, the higher-order model developed here produce at breaking waves solutions which are close to that obtained with Saint Venant equations. In the ensuing tests, these results are generalized for shallow flows over uneven beds, e.g., at obstacles in a stream.

3 Numerical method

Equations (7) and (15) are rewritten after some mathematical manipulations as follows

$$\frac{\partial \mathbf{W}}{\partial t}+\frac{\partial \mathbf{F}}{\partial x}=\mathbf{S}_o+\mathbf{S}_d+\mathbf{S}_p, \tag{25}$$

where the vector of unknows $\mathbf{W}$, flux vector $\mathbf{F}$ and source terms are

$$\begin{aligned}
&\mathbf{W}=\begin{pmatrix} h\\ \sigma\end{pmatrix}, \quad \mathbf{F}=\begin{pmatrix} Uh\\ U^2h+\frac{1}{2}gh^2\end{pmatrix},\\
&\mathbf{S}_o=-\frac{\partial z_b}{\partial x}\begin{pmatrix} 0\\ gh\end{pmatrix}, \quad \mathbf{S}_d=-\frac{\partial \tilde{D}}{\partial x}\begin{pmatrix} 0\\ 1\end{pmatrix}-\frac{\partial B}{\partial x}\begin{pmatrix} 0\\ 1\end{pmatrix},\\
&\mathbf{S}_p=-\frac{\partial z_b}{\partial x}\begin{pmatrix} 0\\ \tilde{p}_1/\rho\end{pmatrix}-\frac{\partial z_b}{\partial x}\begin{pmatrix} 0\\ p_2/\rho\end{pmatrix}.
\end{aligned} \tag{26}$$

Here

$$\begin{aligned}
\sigma &= Uh-\frac{1}{3}h^3U_{xx}-h^2U_xh_x+Uhz_{bx}\left(z_{bx}+h_x\right)+\frac{1}{2}Uh^2z_{bxx},\\
\tilde{D} &= \left(U_x^2-UU_{xx}\right)\frac{1}{3}h^3+\left(U^2z_{bxx}+UU_xz_{bx}\right)\frac{1}{2}h^2+(Uh)_x\left(Uz_{bx}-hU_x\right)h,\\
\frac{\tilde{p}_1}{\rho} &= \left(U_x^2-UU_{xx}\right)\frac{1}{2}h^2+\left(U^2z_{bxx}+UU_xz_{bx}\right)h+(Uh)_x\left(Uz_{bx}-hU_x\right).
\end{aligned} \tag{27}$$

The terms B and p_2 are given by Eqs. (19) and (21), respectively. Note that the time derivatives in Eq. (25) are collected in a single term for the time-stepping [14].

A high-resolution scheme was implemented for the solution of Eq. (25). The time stepping is conducted using a third-order Strong Stability-Preserving (SSP) Runge–Kutta scheme as follows [40]:

$$\begin{aligned}
&\mathbf{W}_i^{(1)}=\mathbf{W}_i^k+L\left[\mathbf{U}_i^k\right]\Delta t+(\mathbf{S})_i^k\Delta t \Rightarrow \mathbf{U}_i^{(1)}=E\left[\mathbf{W}_i^{(1)}\right]^{-1},\\
&\mathbf{W}_i^{(2)}=\mathbf{W}_i^{(1)}+L\left[\mathbf{U}_i^{(1)}\right]\Delta t+(\mathbf{S})_i^{(1)}\Delta t \Rightarrow \mathbf{U}_i^{(2)}=E\left[\mathbf{W}_i^{(2)}\right]^{-1},\\
&\mathbf{W}_i^{(3)}=\frac{3}{4}\mathbf{W}_i^k+\frac{1}{4}\mathbf{W}_i^{(2)} \Rightarrow \mathbf{U}_i^{(3)}=E\left[\mathbf{W}_i^{(3)}\right]^{-1},\\
&\mathbf{W}_i^{(4)}=\mathbf{W}_i^{(3)}+L\left[\mathbf{U}_i^{(3)}\right]\Delta t+(\mathbf{S})_i^{(3)}\Delta t \Rightarrow \mathbf{U}_i^{(4)}=E\left[\mathbf{W}_i^{(4)}\right]^{-1},\\
&\mathbf{W}_i^{k+1}=\frac{1}{3}\mathbf{W}_i^k+\frac{2}{3}\mathbf{W}_i^{(4)} \Rightarrow \mathbf{U}_i^{k+1}=E\left[\mathbf{W}_i^{(k+1)}\right]^{-1},
\end{aligned} \tag{28}$$

where $\mathbf{S}=\mathbf{S}_d+\mathbf{S}_p$ and Δt is the time step. Here $E[]$ is an elliptic operator linked to the discrete version of σ [see Eq. $(27)_1$], and $L()$ is a finite-volume spatial operator [4]

$$L(\mathbf{U}_i) = -\frac{1}{\Delta x}\left(\mathbf{F}_{i+1/2} - \mathbf{F}_{i-1/2}\right) + \mathbf{S}_{oi}, \tag{29}$$

where $\mathbf{F}_{i+1/2}$ is the numerical flux crossing the interface $i+1/2$ of cell i and Δx is the cell width. The space operator $L()$ uses $\mathbf{U}$ reconstructed with 4th-order accuracy, given the high-order dispersive effects to be modeled. The elliptic operator $E[]$ is discretized with second-order finite-differences to preserve a tridiagonal structure and ensure a fast inversion of the linear system of equations determining the non-hydrostatic velocity field. A 4th-order total variation diminishing monotone upstream centered scheme for conservation laws (MUSCL-TVD-4th) is adopted to reconstruct the solution [41]. The local Riemann problem at each cell interface is then determined by the vector $\mathbf{U}$ at its the left (L) and right (R) sides from

$$\mathbf{U}^L_{i+1/2} = \mathbf{U}_i + \frac{1}{6}\left[\xi(r_1)\Delta^*\mathbf{U}_{i-1/2} + 2\xi\left(\frac{1}{r_1}\right)\Delta^*\mathbf{U}_{i+1/2}\right], \tag{30}$$

$$\mathbf{U}^R_{i+1/2} = \mathbf{U}_{i+1} - \frac{1}{6}\left[2\xi(r_2)\Delta^*\mathbf{U}_{i+1/2} + \xi\left(\frac{1}{r_1}\right)\Delta^*\mathbf{U}_{i+3/2}\right], \tag{31}$$

where the operators used are defined as follows

$$\Delta^*\mathbf{U}_{i+1/2} = \Delta\mathbf{U}_{i+1/2} - \frac{1}{6}\left(\Delta\overline{\mathbf{U}}_{i+3/2} - 2\Delta\overline{\mathbf{U}}_{i+1/2} + \Delta\overline{\mathbf{U}}_{i-1/2}\right), \tag{32}$$

$$\Delta\overline{\mathbf{U}}_{i-1/2} = \mathrm{minmod}[\Delta\mathbf{U}_{i-1/2}, \Delta\mathbf{U}_{i+1/2}, \Delta\mathbf{U}_{i+3/2}], \tag{33}$$

$$\Delta\overline{\mathbf{U}}_{i+1/2} = \mathrm{minmod}[\Delta\mathbf{U}_{i+1/2}, \Delta\mathbf{U}_{i+3/2}, \Delta\mathbf{U}_{i-1/2}], \tag{34}$$

$$\Delta\overline{\mathbf{U}}_{i+3/2} = \mathrm{minmod}[\Delta\mathbf{U}_{i+3/2}, \Delta\mathbf{U}_{i-1/2}, \Delta\mathbf{U}_{i+1/2}], \tag{35}$$

$$\Delta\mathbf{U}_{i+1/2} = \mathbf{U}_{i+1} - \mathbf{U}_i. \tag{36}$$

Herein, the minmod function is given by

$$\mathrm{minmod}[a,b,c] = \mathrm{sign}(a)\max\left[|a|, 2\mathrm{sign}(a)b, 2\mathrm{sign}(a)c\right]. \tag{37}$$

The Van-Leer limiting function is used here

$$\xi(r_i) = \frac{r_i + |r_i|}{1 + |r_i|}, \quad r_1 = \frac{\Delta^*\mathbf{U}_{i+1/2}}{\Delta^*\mathbf{U}_{i-1/2}}, \quad r_2 = \frac{\Delta^*\mathbf{U}_{i+3/2}}{\Delta^*\mathbf{U}_{i+1/2}}. \tag{38}$$

The surface gradient method is applied to reconstruct the water surface elevation, and once the reconstruction step is finished, the numerical flux $\mathbf{F}_{\mathrm{i}+1/2}$ is estimated with the HLL approximate Riemann solver [4]:

$$\mathbf{F}_{i+1/2} = \begin{cases} \mathbf{F}_L & \text{if } S_L \geq 0 \\ \dfrac{S_R\mathbf{F}_L - S_L\mathbf{F}_R + S_R S_L\left(\mathbf{U}_R - \mathbf{U}_L\right)}{S_R - S_L} & \text{if } S_L \leq 0 \leq S_R \\ \mathbf{F}_R & \text{if } S_R \leq 0 \end{cases} \tag{39}$$

Here $\mathbf{F}_L$ and $\mathbf{F}_R$ are the fluxes computed at states L and R. Robust wave speed estimates S_L and S_R for wet and dry bed conditions are considered following Toro [4], and the topography source term is discretized ensuring a well-balanced scheme [32]. The time stepping procedure is adaptative based on the Courant-Friedrichs-Lewy number CFL as follows:

$$\Delta t = \mathrm{CFL}\left[\frac{\Delta x}{\max\left|U_i^k\right| + \left(g h_i^k\right)^{1/2}}\right], \tag{40}$$

with CFL < 1 for stability. The dispersive terms in the source term **S** are discretized using fourth-order accurate central finite-differences (Table 1) for the computational cells $i=3$ to $N-2$, where N is the total number of cells. Near shocks the discrete version of the terms B and p_2 produced high-frequency secondary numerical oscillations, that are supressed by using a 3-point moving average filter. At the cells $i=2$ and $N-1$, the terms in **S** are discretized using second-order differences. For example, the depth-averaged velocity derivatives are given by

$$\left(\frac{\partial^m U}{\partial x^m}\right)_i = \frac{1}{\Delta x^m}\sum_{-k}^{+k}\omega_k U_k + \mathrm{O}(\Delta x^n), \tag{41}$$

with the various coefficients available in Table 1.

Boundary conditions are implemented using ghost cells at $i=1$ and $i=N$ as follows, for the test cases considered in the ensuing section. At the upstream boundary the physical discharge entering the flume is prescribed, and the water depth is obtained by a zero-order extrapolation from the interior solution as $h_1=h_2$. If the upstream section is an open boundary, then the discharge is determined as $q_1=q_2$. If the upstream boundary section is a solid wall, reflective conditions $h_1=h_2$ and $q_1=-q_2$ are implemented. At the outflow section an open boundary is implemented using transmissive conditions $h_N=h_{N-1}$ and $q_N=q_{N-1}$. In the case of water depth regulation at the tailwater section of the channel, h_N is set equal to the experimentally determined water depth.

Table 1 Weighting factors for discretization of spatial derivatives in non-hydrostatic terms [42]

Order of derivative m	Order of accuracy n	Weighting factor ω_k at nodes				
		$k=-2$	$k=-1$	$k=0$	$k=+1$	$k=+2$
1	2	0	−1/2	0	+1/2	0
1	4	1/12	−2/3	0	2/3	−1/12
2	2	0	1	−2	1	0
2	4	−1/12	4/3	−5/2	4/3	−1/12

4 Test cases

4.1 Flow adjustment over an isolated ridge

An experimental procedure to generate waves evolving over an obstacle consists in rapidly accelerate to a constant velocity an obstacle initially at rest in a flume filled with water [43, 44] (Fig. 2a). In Long's [44] experimental work, the obstacle was moved in the flume by a thin line wrapped around a cylindrical winder driven by a motor. The velocity of obstacle displacement was experimentally determined by counting the revolutions, and then this velocity was used to deduce the flow patterns for an observer moving with the obstacle, e.g., the equivalent flow with a static obstacle [44] (Fig. 2b). The initial conditions in Long's experiments are thus $h(x, 0) = h_o - z_b(x)$ and $U(x, 0) = U_o$. During the time-dependent flow adjustment over the obstacle, waves are formed moving upstream and downstream of the obstacle [1, 6, 7, 43, 44] (Fig. 2b).

The upstream non-breaking waves are generally non-hydrostatic unless the topography be very gentle. Breaking waves are typically observed at the lee side of the obstacle (Fig. 2b). If the flow changes from sub- to supercritical conditions along the obstacle, then non-hydrostatic conditions prevail at the hump crest in a rapidly varying topography [2, 19, 45].

Nadiga et al. [1] considered Long's flow adjustment test and conducted a numerical study by comparing solutions of the Serre–Green–Naghdi (SGN) equations with the full non-hydrostatic solutions based on the Euler equations. Their simulations with the SGN equations showed inability of this shallow-water representation to realistically reproduce the lee-side waves, given that wave breaking is not modeled. However, the SGN equations showed excellent reproduction of the dispersive non-breaking waves moving upstream. The bed profile considered by Nadiga et al. [1] is the smooth sill of equation

$$z_b = a\left[1 + \left(\frac{x}{L}\right)^2\right]^{-3/2}, \tag{42}$$

Fig. 2 Flow adjustment over isolated ridge **a** Long's [43, 44] experiments, **b** Equivalent time-dependent flow with static obstacle applying a velocity $-U_o$ to the system

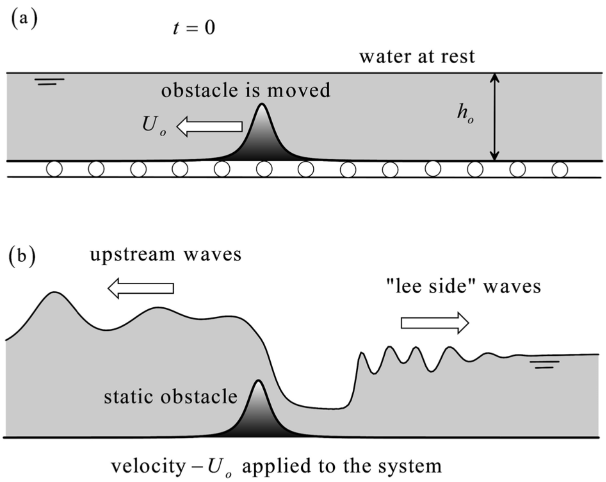

where a is the maximum elevation of the sill and L is a bed-form width parameter. We consider the solution of the Euler equations by Nadiga et al. [1] and compare it with the solution of our new Su-Gardner (SG) equations. For reference, solutions of the SGN and SV equations are also produced, thereby presenting a general comparison of these three shallow-water representations.

Figure 3 considers a test with a stringent topography shape defined by $a=0.65h_o$ and $L=h_o$, with upstream flow conditions given by $\mathrm{F}_o=U_o/(gh_o)^{1/2}=0.7$. Solutions of the SG and SGN equations are presented at normalized times $T=t/t_o$, with $t_o=(h_o/g)^{1/2}$, of 10, 20 and 30 in Fig. 3a–c, respectively, and compared with the full 2D solution. Simulations were conducted using $\Delta x=0.01$ m and CFL $=0.5$. In this test case boundaries are open. On inspecting Fig. 3 it can be observed that the SGN and SG equations yield almost identical results for the upstream waves, which are in excellent agreement with the Euler equations. It means the main contribution to the solution from dispersive corrections is due to D and p_1, such that B and p_2 are not relevant there. On the other hand, the lee side waves are poorly reproduced by the SGN equations, with an evident wave breaking observed in the full Euler solution, not accounted for by them. In contrast, the SG equations produces a significant improvement in the prediction of the lee side waves, with the maximum and minimum water depths roughly close to those predicted by the Euler system. Note the ability of the SG equations to mimic wave breaking by introducing shocks in the solution, a feature fully lacking in the SGN equations.

The same test is considered in Fig. 4, but inserting simulations using the SV equations instead of that of the SGN equations. It can be observed that the solution of the SG equations for the lee side waves tend to produce a shock-like solution similar to that of the SV equations, thus in better agreement with the Euler equations than the solution produced with the SGN equations. Along the obstacle, water depths are overpredicted upstream and under predicted downstream by the SV equations, given that the vertical acceleration is not accounted for. The upstream wave predicted by the SV equations is a shock, which is not in agreement with the Euler equations. Collectively, Figs. 3 and 4 reveal that the SGN equations produce a good solution upstream and along the obstacle, whereas the SV produce a good representation of the lee side waves. In contrast, the new SG equations developed in this work produce a solution in good conformity with the Euler equations along the whole computational domain. To our knowledge, there was so far not any Boussinesq-type shallow water representation in the literature with such capabilities.

Based on the above observations, it emerges the rationale of a family of models widely used for non-hydrostatic modeling, namely, to construct hybrid models combining the SGN-SV equations. The broken surges and their energy dissipation are well characterized by the shocks produced by the solution of the SV equations, while long non-breaking waves are accurately described by the SGN equations. Thus, the SGN equations are solved and switch locally to the SV equations in those portions of the wave where breaking is detected [27, 28]. The SGN-SV hybrid models use breaking modules depending on the calibration of three parameters, namely the free surface slope at the onset of breaking, a factor relating the rate of variation of the flow depth to the long wave celerity at the onset of breaking and the limiting Froude number for initiation of roller development at a broken wave. These three parameters are case-dependent. Further, patching of SGN and SV equations at the wave breaking zones involve numerical instabilities during mesh refinement [29], sometimes difficult to control in a model. In contrast, the new SG equations presented are free from calibration parameters. Wave breaking is mimicked trough shock-like waves resulting from a balance between the dispersive terms arising in the Serre–Green–Naghdi theory and the high-order non-linear terms originating from the differential advection of

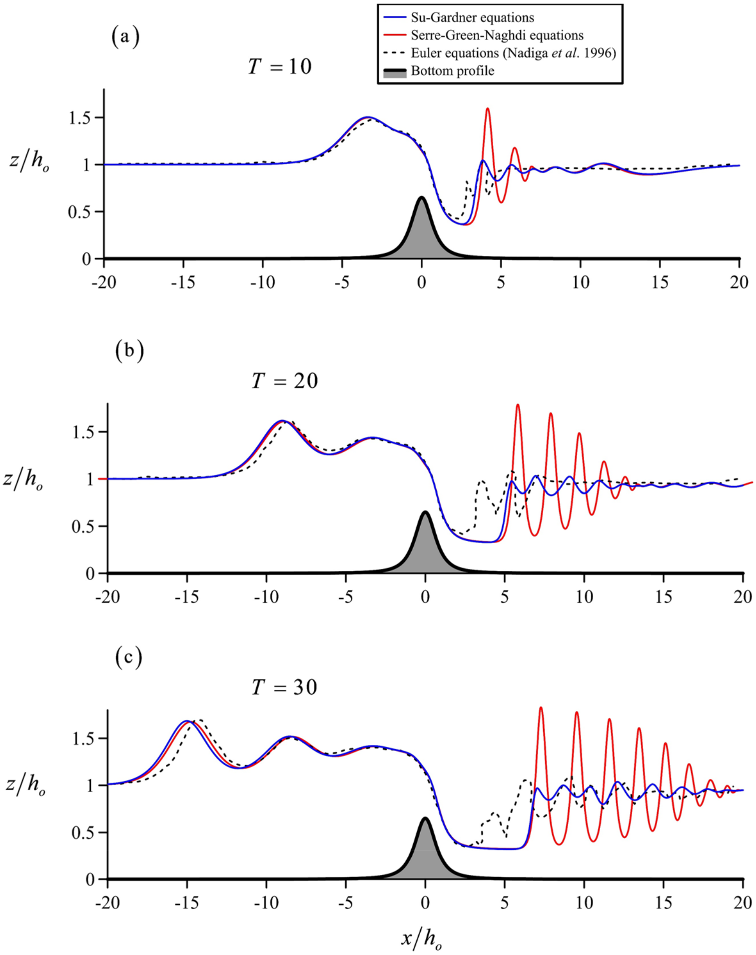

Fig. 3 Flow adjustment over isolated ridge: Comparison of SG equations with SGN equations and Euler equations. Test conditions: $F_o = 0.7$, $a/h_o = 0.65$, $L/h_o = 1$

momentum and the supplemental vertical acceleration due to the non-uniform velocity profile.

Figures 5 and 6 considers a test with a topography shape determined from $a = 0.4h_o$ and $L = h_o$, with upstream critical flow conditions as by $F_o = U_o/(gh_o)^{1/2} = 1$. Solutions of the SG and SGN equations are presented at normalized times T of 10, 20 and 30 in Fig. 5a–c, respectively, and compared with the full 2D solution, whereas the SV solutions are available in Fig. 6. Simulations were conducted using $\Delta x = 0.01$ m and CFL = 0.5. In this test, wave breaking at the lee side waves is not as strong in the SG equations as indicated by the Euler equations. This is a limitation of the SG modeling approach, given that wave breaking is not an impulsive and fast process, but rather occurs gradually in the SG shallow water approximation [25]. Nevertheless, the lack of any calibration parameter makes it useful in spite of the limitations. As in the former test, SGN and SG solutions are similar for the upstream waves and in overall conformity with the Euler equations, whereas the SV solution is unrealistic. For the lee side waves,

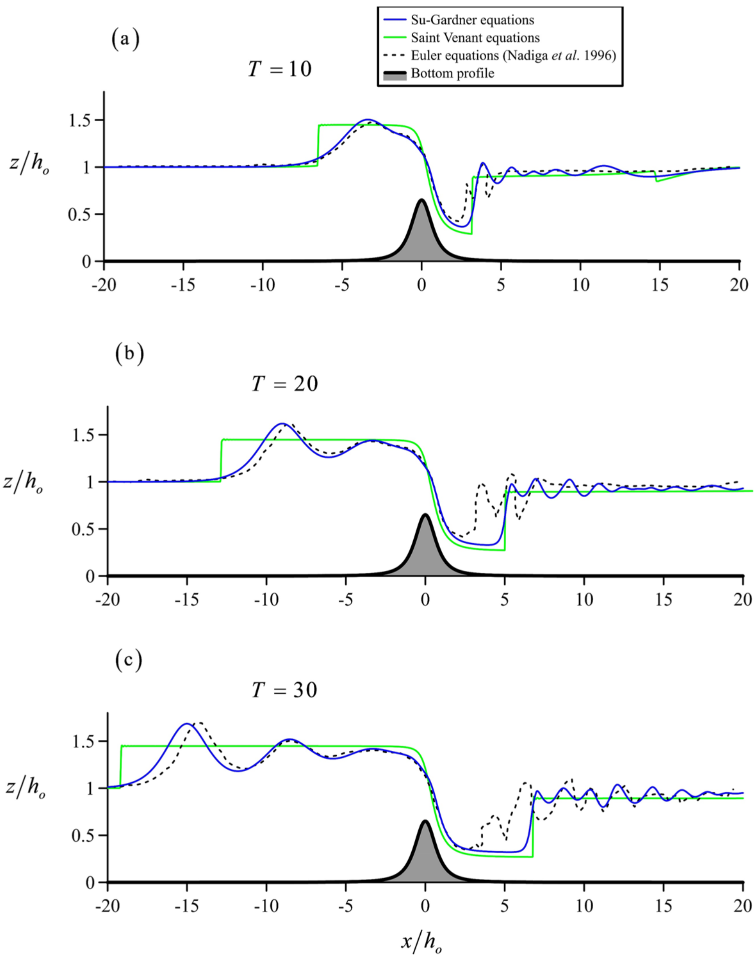

Fig. 4 Flow adjustment over isolated ridge: Comparison of SG equations with SV equations and Euler equations. Test conditions: $F_o = 0.7$, $a/h_o = 0.65$, $L/h_o = 1$

SGN equations are not in conformity with the Euler equations, but the SG equations are closer.

The current analysis of the SG solutions for Long's flow adjustment test demonstrates the utility of the SG equations to predict shallow water waves over obstacles: it is a single high-order shallow water representation that has the best features of each of its germane lower-order representations, namely SGN and SV approximations.

4.2 Dam break wave propagating over a bottom sill

Ozmen-Cagatay and Kocaman [46] conducted experiments in a horizontal flume of 8.9 m long, 0.3 m width and 0.34 m deep, consisting in dam-break flows simulated with a $h_o = 0.25$ m flow depth pool retained by a gate with dry bed conditions downstream (Fig. 7a). This problem was previously investigated experimentally by Soares Frazão and

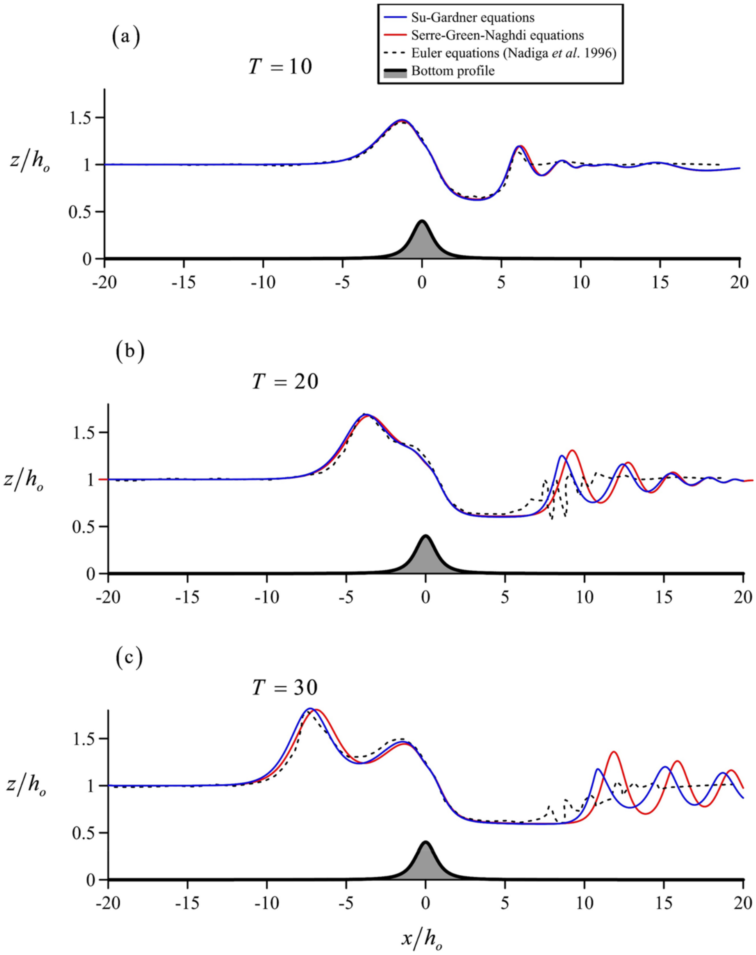

Fig. 5 Flow adjustment over isolated ridge: Comparison of SG equations with SGN equations and Euler equations. Test conditions: $F_o = 1$, $a/h_o = 0.4$, $L/h_o = 1$

Zech [47]. In this test case the upstream boundary is a solid wall, and the downstream boundary is open. A symmetrical trapezoidal sill of 0.075 m height, 0.30 m crest length and 1 V:4.67H side slope was placed downstream of the gate [46]. Once the gate was opened fast, a dam break front propagated towards and over the obstacle (Fig. 7b), resulting a negative surge generation over the sill crest, as observed in the experiments [46].

These are plotted in Fig. 8., along with Reynolds-Averaged Navier–Stokes (RANS) solutions, consisting in instantaneous flow profiles at times $T = 11.9$, 17.54, 20.67, 23.05, 29.69 and 41.84 [46]. Note that the RANS solutions [46] predict a correct formation of the surge over the obstacle ($T = 11.9$ and 17.5), whereas some disagreement with experiments is noted at the onset of wave breaking ($T = 20.67$). Overall, the process is very well described by the RANS solutions, including the negative surge formation, celerity of propagation in the upstream direction, and flow depth profiles. Thus, we consider the RANS

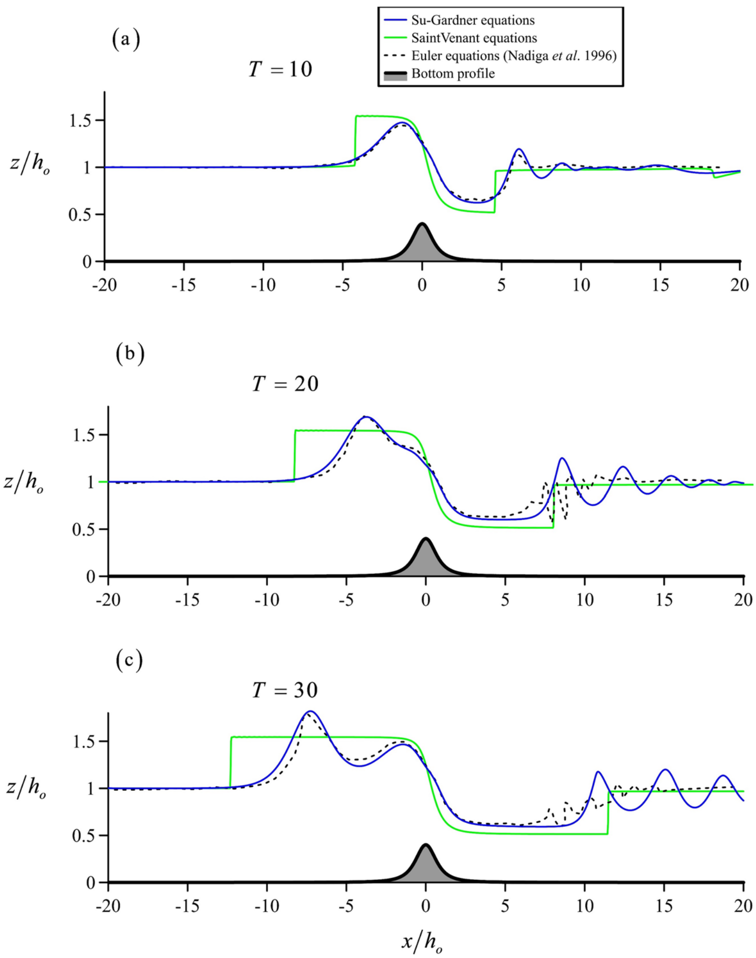

Fig. 6 Flow adjustment over isolated ridge: Comparison of SG equations with SV equations and Euler equations. Test conditions: $F_o = 1$, $a/h_o = 0.4$, $L/h_o = 1$

solutions as reference to evaluate the different shallow water approximations considered in this work.

Simulations were conducted with the SG, SGN and SV equations using $\Delta x = 0.01$ m and CFL = 0.5. The results for each of the shallow water approximations are compared with experiments and RANS simulations [46] in Figs. 8, 9 and 10, respectively. On inspecting Fig. 8 it can be observed that the surge development over the obstacle is very well predicted by the SG equations, with a notable agreement with RANS solutions at times $T = 11.9$, 17.54, 20.67 and 23.05. The predicted celerity of the surge is also in good agreement with experiments and the RANS equations. At $T = 29.69$ the wave breaking simulated by the SG equations is less than that in the RANS solutions, as is also evident at $T = 41.84$ by the small train of waves moving upstream behind the surge. However, given that our simulations are conducted assuming inviscid flow without any turbulence accounted for, the results are considered satisfactory. Note the excellent prediction of the flow profile over

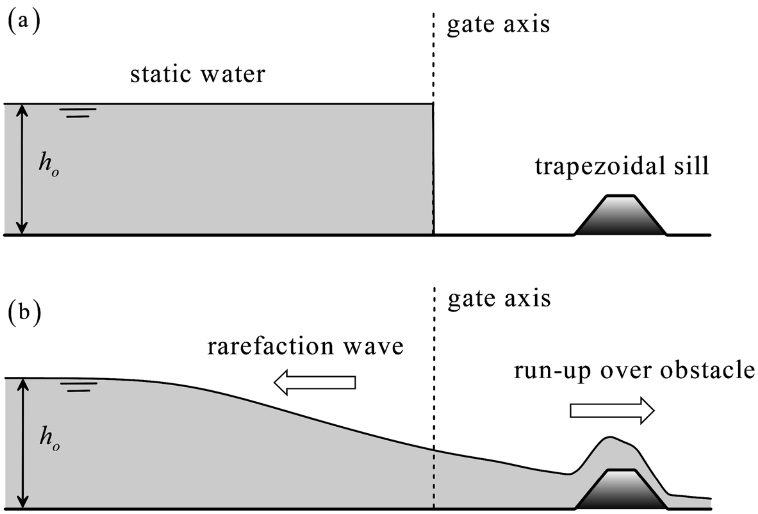

Fig. 7 Dam-break wave propagating over a bottom sill **a** initial condition, **b** wave patterns generated

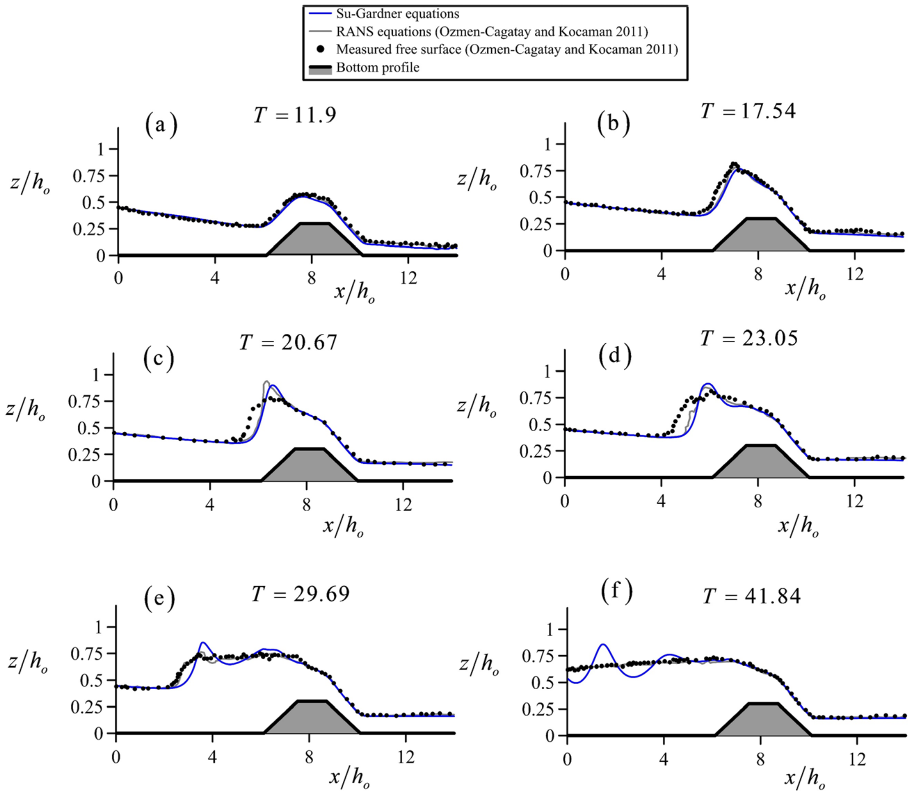

Fig. 8 Dam break wave propagating over a sill at different instants of time: Comparison of SG equations with RANS equations and experiments [46]

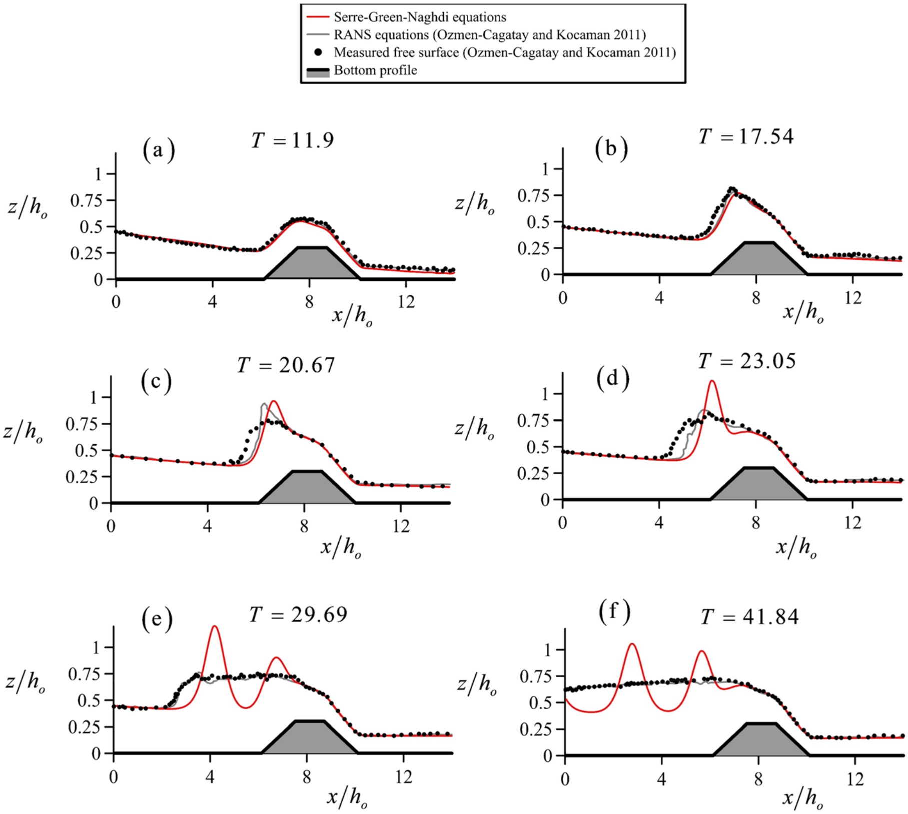

Fig. 9 Dam break wave propagating over a sill at different instants of time: Comparison of SGN equations with RANS equations and experiments [46]

the obstacle by the SG equations at $T=41.84$. Figure 9 contains the germane simulations using the SGN equations. At times $T=11.9$ and 17.54 results are almost identical to those obtained with the SG equations, but at later times the SGN solutions deviate from the SG solutions and thus become unreliable. Note the surge formation is poorly predicted at times $T=20.67$ and 23.05, and the incorrect prediction of the upstream free surface profile, and at the obstacle inlet ($T=29.69$ and 41.84). Comparison of Figs. 8 and 9 depicts the significant advance of using the SG equations instead of the SGN equations. We remark again that the whole surge formation and breaking process result of our simulations with the SG equations is a consequence of the shallow water approximation used ab-initio, without introducing any empirical case-dependent parameter.

Finally, simulations for this same test case using the SV equations are presented in Fig. 10. The surge development at $T=17.54$, 20.67 and 23.05 is not in very good agreement with RANS solutions. However, a major advantage of this shallow water approximation is in the representation of surges as shocks in the solution. Note that the solutions at times $T=29.69$ and 41.84 are reasonably good for the upstream surge. A failure of this approximation occurs at the obstacle, given that the SV equations fail to simulate flows with non-hydrostatic flow conditions. The flow profile simulated by the SG, SGN, and SV over the sill crest is detailed in Fig. 11, where the advantages of the SG equations are

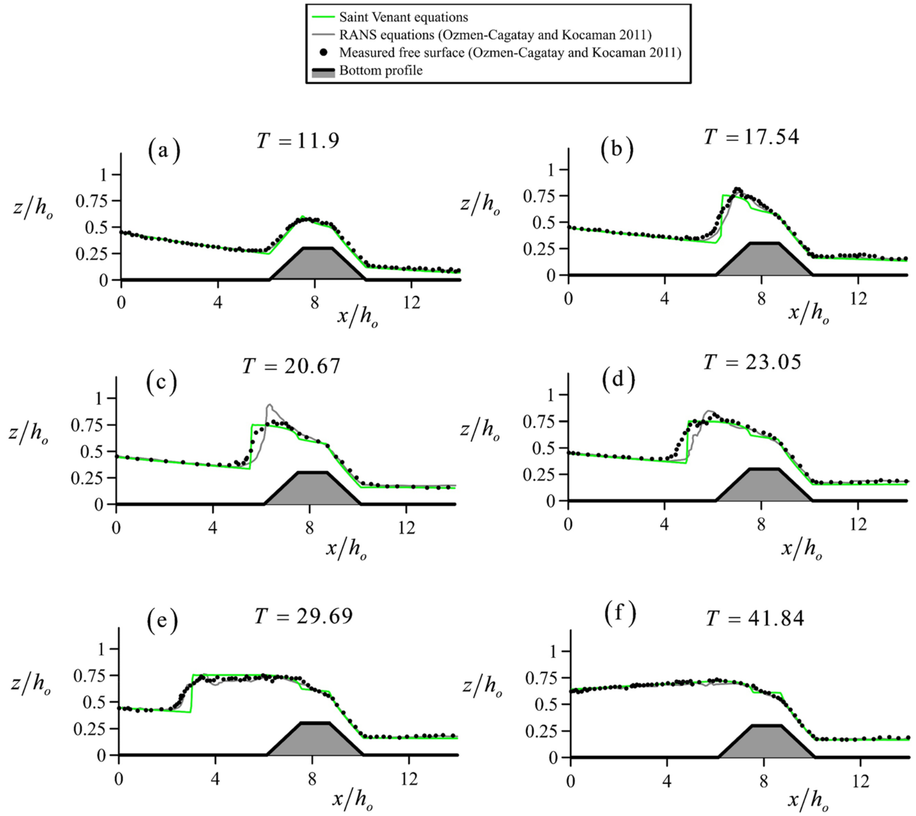

Fig. 10 Dam break wave propagating over a sill at different instants of time: Comparison of SV equations with RANS equations and experiments [46]

evident. The SV equations produced an unrealistic profile over the sill crest with an almost constant water depth distribution. The SGN equations produced an acceptable flow profile over the sill crest, but an unreliable solution at the sill inlet, with cnoidal-type waves. The SG approximation produces an excellent non-hydrostatic flow profile both at the inlet and sill crest.

4.3 Steady flow over submerged bar

Cienfuegos et al. [39] developed the model SERR-1D, which is a high-resolution TVD solver for the solution of the Serre–Green–Naghdi equations. This program was used by Mignot and Cienfuegos [48] to study river-like flows. The model accounted for by wave breaking using an eddy-viscosity approach, with various calibration parameters tunned conducting maritime hydraulics test cases. They presented a relevant test case to validate the ability of a non-hydrostatic model to simulate hydrostatic flows over uneven beds. This occurs in steady submerged flows over wide topographical obstacles with small overflow depths. This problem was also discussed by Nadiga et al. [1]. The topography used is given by the submerged bar of equation

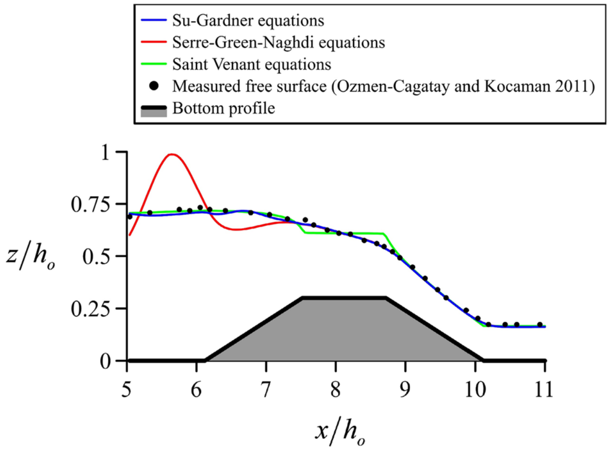

Fig. 11 Comparison of different shallow water approximations at the sill crest ($T = 41.84$)

$$z_b = 0.2\left[1 - \left(\frac{x - 15}{4}\right)^2\right]. \tag{43}$$

Simulations were conducted with identical conditions to those used by Mignot and Cienfuegos [48]. Boundary conditions for this test consists in a water depth of 0.48 m at the downstream end of the channel reach and a unit discharge of $q = 0.3$ m^2/s at the inflow section. The channel length considered is 30 m, and $\Delta x = 0.1$ m was used for the cell width. The time stepping was conducted with CFL = 0.5. Simulations obtained with the SG and SV equations are plotted in Fig. 12 and compared with the results of the SERR-1D model reported by Mignot and Cienfuegos [48].

Our solution of the SV equations was verified to perfectly match that presented by Mignot and Cienfuegos [48]. Note the flow is essentially hydrostatic throughout the channel, with the solution of the SV equations and SERRE-1D model in excellent agreement, except in the hydraulic jump position over the bar. Mignot and Cienfuegos [48] attributed this discrepancy to a possible vias in the celerity estimation of the surge by the SERRE-1D model during the flow adjustment over the obstacle towards the steady state. It was indicated that a reconsideration of the calibration parameters in the model could be a means

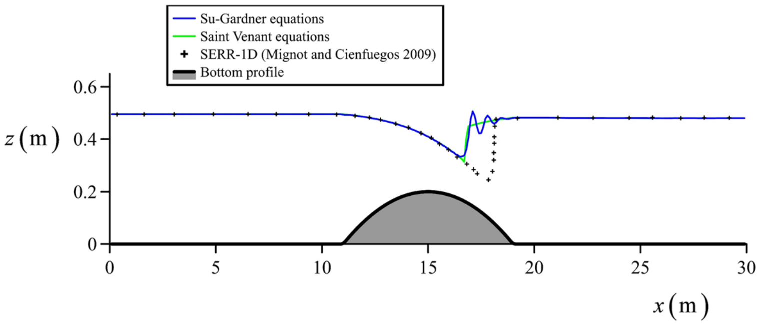

Fig. 12 Steady flow over submerged bar: Comparison of SG equations with SV equations and results from the SERRE-1D model [48]

to improve predictions. Our simulation with the SG equations predicts the surge celerity correctly, thus its final position is in excellent agreement with the SV equations (Fig. 12). Some secondary oscillations are present in the SG solution, given that wave breaking in the model is progressive, as previously indicated. However, given the lack of calibration parameters, the result is considered satisfactory.

Nadiga et al. [1] also considered simulations using the SGN equations for flow conditions where the correct solutions shall be hydrostatic along the computational domain. Steady flow over a wide submerged bar with with $F_o = 0.45$, $a/h_o = 0.5$ and $L/h_o = 5$ is depicted in Fig. 13a. Here, solutions of the SGN and SV equations are compared. This is a wide topography; thus, hydrostatic flow should prevail thorough. However, note the extremely large dispersive corrections generated by the SGN equations in the form of an undular hydraulic jump. This portion of the flow profile is obviously unrealistic, pointing out a strong limitation of the SGN equations, given that the undular jump waves should break. Undular flows are possible downstream of a weir [49], but such undulations cannot be arbitrary, as those found here with the SGN equations. The undular hydraulic jump is physically possible (roughly) for inflow Froude numbers less than 1.7 [50], resulting in adequate predictions by using Boussinesq equations [51]. However, for larger Froude numbers the undular waves will break, and a roller is formed on the free surface [52].

The simulation conducted with the new SG equations is presented in Fig. 13b, resulting an excellent agreement with the SV equations along the whole computational domain. Note the excellent approximation to the hydraulic jump profile at the lee side of the bar. The small ripples noted on the flow profile there are the result of a progressive breaking of the undular waves that the usual dispersive corrections tend to form in the solution. Thus,

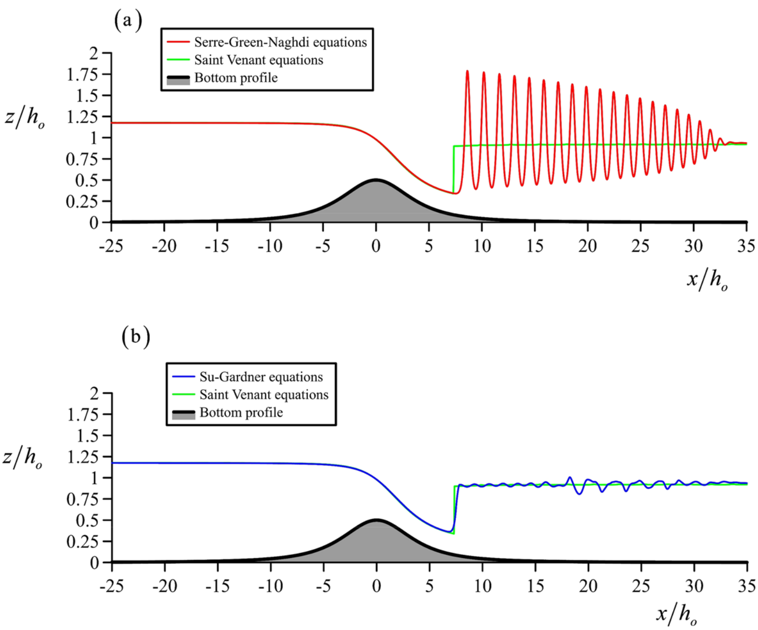

Fig. 13 Steady flow over submerged bar with $F_o = 0.45$, $a/h_o = 0.5$, $L/h_o = 5$ **a** comparison of SGN and SV equations, **b** comparison of SG and SV equations

the SG equations allows a better representation of steady hydraulic jumps than the SGN equations.

Experiments on hydraulic jumps over curved bed obstacles seems to be lacking in the literature to the authors' knowledge. Thus, a new set of experiments were conducted in a 15-m-long, 1-m-high, 1-m-width tilting experimental flume at the Hydraulics laboratory of the University of Córdoba, Spain, to generate steady hydraulic jumps at the lee side of obstacles. The flume width is reduced to 0.405 m by a moving division wall (Fig. 14a), and the flume slope for the experimental series conducted is 0.0015 m/m. The tailwater portion of the flume from 9.634 to 15 m downstream of the inlet section is structurally a cantilever ending in a water tank, and the beam deformation, though very small, was considered to accurately define the actual bed profile of the flume. The flume is equipped with a recirculation pump of 0.078 m^3/s maximum discharge connected to the downstream water tank, allowing to work in closed-circuit. A water tank with flow straightener is located at the flume inlet to reduce flow disturbances. A large-scale obstacle model of equation (dimension in meters)

$$z_b = 0.209\exp\left[-\frac{1}{2}\left(\frac{x-6.565}{0.254}\right)^2\right], \tag{44}$$

is installed upstream from the middle portion of the flume (Fig. 14a). Flow visualization during the experiments was accomplished through the eight lateral crystal windows of 1.875-m-wide by 0.975-m-high of the flume. Each window was monitored by a camera perpendicularly installed in front of the flume. The monitoring video system comprises eight Basler Ace acA1920-40uc cameras, with 6 mm focal length lens to allow capturing the whole width of each lateral crystal window, 40 frames-per-second (fps) maximum at full resolution, and a laptop Intel® Core™ i7-9750H with software for image capture, synchronization, assembling and processing. The system automatically assembles the images collected by the 8 cameras in a synchronized way, correcting distortion errors and thereby providing instantaneous experimental images for the 15 m of flume. To produce a steady transcritical flow over the obstacle, a discharge Q was supplied at the inlet by manual regulation of a valve. An ultrasonic flowmeter installed in the recirculation conduit allows for discharge measurements within $\pm 0.4\%$ accuracy. The water levels downstream of the obstacle were regulated with a tailgate, that allowed to control the position of the hydraulic jump. Once the images collected by the system of cameras were assembled and distortion errors were corrected for selected instants of time, they were used to extract the experimental flow profile. Although the flow was globally steady in the experiments, at the hydraulic jumps the free surface involves instantaneous fluctuations. Thus, an averaged flow profile was determined from images at five different instants of time. Four steady flow profiles were measured, and the results are plotted in Fig. 14b-e. From panel b to panel e the tailwater level is progressively increased by closing the tailgate, thus the hydraulic jump moves towards the obstacle. The bed and experimental free surfaces are available as supplemental material to this article.

Simulations were conducted with the SG equations using $\Delta x = 0.02$ m and CFL $= 0.8$. Boundary conditions implemented in the numerical model are the measured steady discharge at the inlet and the measured regulated tailwater level. Friction effects were considered to accurately determine the position of the hydraulic jump by using Manning's equation for the friction slope $S_f = n^2U^2/h^{4/3}$, with $n = 0.01$ $sm^{-1/3}$. In the numerical implementation the friction source term was treated explicitly. Comparison of predictions and experimental measurements in Fig. 14 reveals that the SG equations predicts

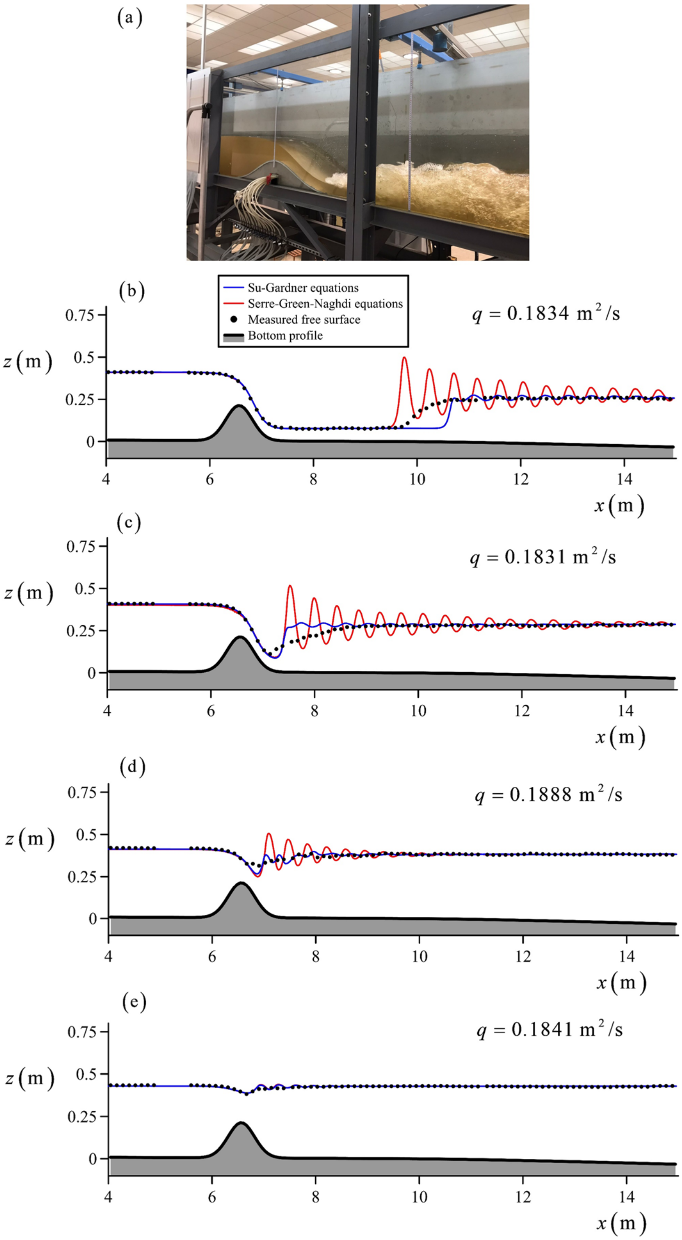

Fig. 14 Hydraulic jumps at the lee side of a large obstacle model **a** general view of experimental set-up at the University of Cordoba, Spain, **b**–**d** comparison of experimental flow profiles with SG and SGN simulations

the free surface profile over the obstacle and hydraulic jump with reasonable accuracy in all cases. Note that the SG equations represent the hydraulic jump as a discontinuity-type solution, thus the length of the hydraulic jump cannot be predicted by this mathematical representation. For comparative purposes the SGN equations were solved for the same experimental tests, and the results are plotted in Fig. 14. This model had to be run with CFL = 0.1 to get stable results once the extremely peaked waves in Fig. 14b formed. Thus, all runs for the SGN model were generated using this low CFL value. Comparison with experiments shows the unrealistic prediction of the hydraulic jump at the lee side of the obstacle for panels (b)-(d) by the SGN model, where it may be noted the large improvement resulting from using instead the SG equations. For panel (e), the obstacle is almost submerged, and the SGN and SG solutions produce nearly identical results. Thus, the new set of experiments presented demonstrate the ability of the SG equations to reproduce steady breaking waves.

4.4 Breaking waves on a slope

Although not properly an obstacle test, the breaking of waves on a slope is an effective test to show the breaking ability of phase resolving models in unsteady flow. Synolakis [53] conducted laboratory experiments for solitary waves running on a plane beach of slope 1:19.85. The crest of the initial solitary wave solution is placed at half a wavelength from the toe of the plane beach (located at $x = 0$ m). A test for a breaking solitary wave run-up with $H/h_o = 0.28$ is presented in Fig. 15, where H is the wave height and h_o the still water depth. Simulations were conducted with the SG equations using $\Delta x = 0.01$ m, CFL = 0.3 and $n = 0.01$ sm$^{-1/3}$. In this test cases boundaries are open. Predictions of the SG equations are compared with experimental data of Synolakis [53] there. Overall, the whole process is well described by our mathematical model, including the wave breaking observed at $T = 20$ and 25, and from $T = 45$ to 60 the moving hydraulic jump progressively formed. Simulations with the SGN equations were found to be unstable for the run-up on the slope.

To show the significant improvement of the SG equations over the SGN equations both approximations are compared prior to the run-up phase at $T = 22$ in Fig. 16. It can be observed the extremely peaked waves predicted by the SGN theory, whereas the effectiveness of the SG equations mimicking breaking is clearly noted. For reference, the solution of the SV at this instant of time is also plotted.

This set of experiments demonstrate the ability of the SG equations to reproduce unsteady breaking waves.

5 Limitations and discussion

The SG equations are a vertically-averaged system of equations originating from Euler equations. The Euler equations are extensively used to study finite amplitude wave propagation and wave breaking problems [37, 54]. The ideal fluid flow assumption makes impossible to simulate the breaking impact after surface reconnection, but the simulation of the onset of breaking events can be carried out with great accuracy [54], with the overturing waves typically determined using volume of fluid or level set methods.

The SG equations are exact in the form stated by Eqs. (7) and (15), but once a velocity field is assumed, the system turns out to be only an approximation to the Euler equations. The practical form of the SG equations used in this work is based on assuming that the velocity field can be approximated by Eqs. (16) and (17), and the limitations stemming from that assumption can be inferred by analyzing the expansion order. These velocity

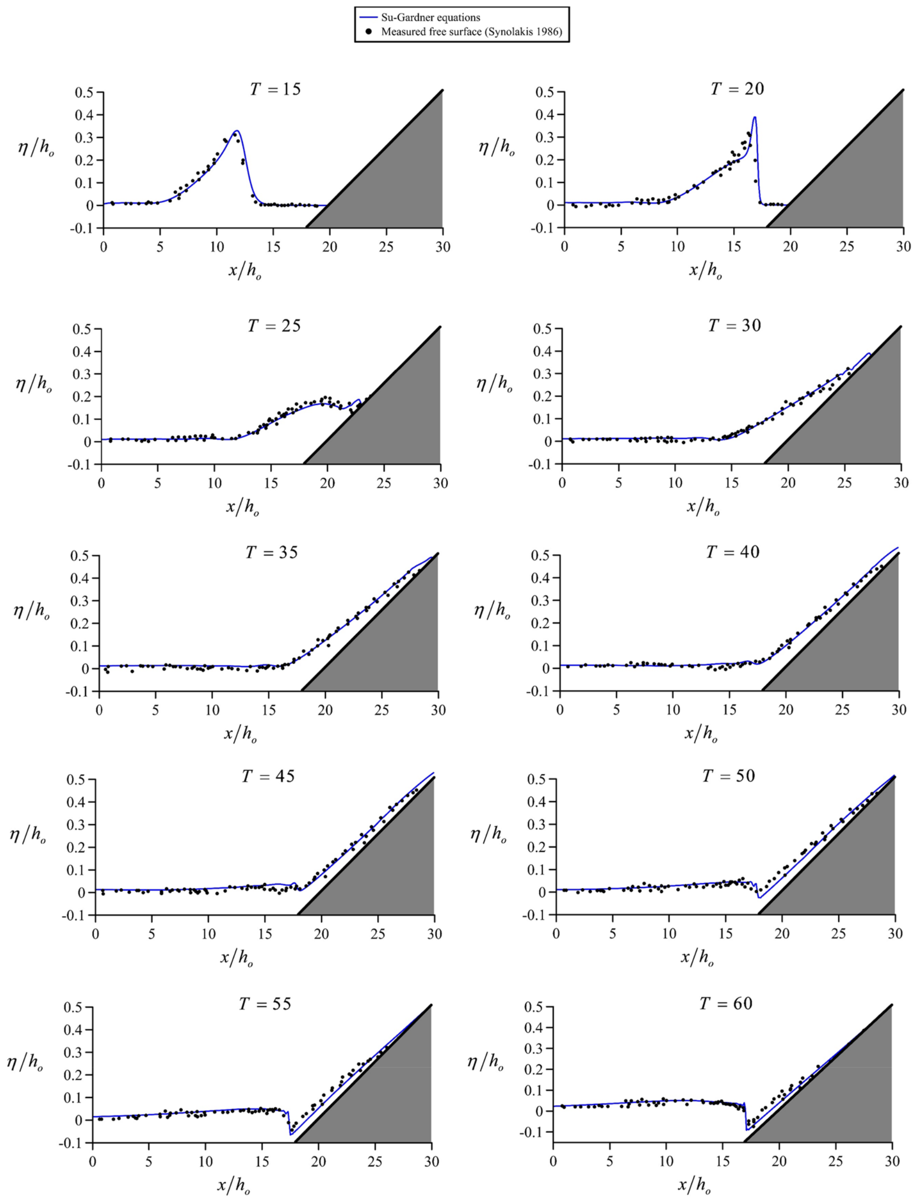

Fig. 15 Breaking solitary wave on a slope. Comparison of experimental flow profiles [52] with SG simulations. Here η is the elevation above the still water level

components are obtained by an iteration of the Cauchy-Riemann equations for irrotational water waves. In the iteration process, Eq. (16) is a result of higher-order than Eq. (17). The stream function ψ compatible to this second-order accurate degree of expansion of the equations of motion is, therefore,

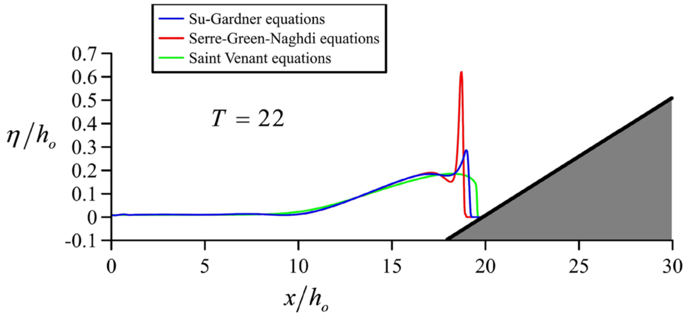

Fig. 16 Comparison of different shallow water approximations for wave breaking on a slope ($T=22$). Here η is the elevation above the still water level

$$\psi(x,z,t) = -U\eta - \left(2U_x z_{bx} h + Uhz_{bxx}\right)\left(\frac{1}{2}\eta^2 - \frac{1}{2}\eta\right) - \left(\frac{1}{2}U_{xx}h^2\right)\left(\frac{1}{3}\eta - \frac{1}{3}\eta^3\right). \quad (45)$$

It can be easily checked that Eq. (45) exactly satisfies the two-dimensional continuity equation, but vorticity appears due to the approximate nature of the solution, given by

$$\omega(x,z,t) = -\left(\frac{\partial^2\psi}{\partial x^2} + \frac{\partial^2\psi}{\partial z^2}\right). \quad (46)$$

For example, for a horizontal bed, the modelled vorticity is found to be given by

$$\omega = \frac{1}{3}U_{xx}z\left(h_x^2 + hh_{xx}\right) + \frac{2}{3}U_{xxx}h_x hz + \frac{1}{6}U_{xxxx}\left(zh^2 - z^3\right). \quad (47)$$

On inspecting Eq. (47) it is observed the dependence of the vorticity on high-order non-hydrostatic terms, thus it will be important at breaking portions of the waves. Therefore, the velocity field used in the SG equations is regarded as an approximation to the Euler equations, with limitations due to the degree of expansion of the stream function, Eq. (45), which is the fundamental approximation underlaying in our method.

An additional aspect that deserves discussion, in addition to the expansion limitations of the approach, is the physical relevance of Eq. (16), e.g., a parabolic profile, to describe the velocity profile at breaking waves and hydraulic jumps. Physical experiments [55–57] indicates that the $u(x, z)$ velocity profile at hydraulic jumps encompasses a complex variation with elevation, involving a backward flow velocity at the free surface. To approximate this velocity profile analytically, experimental results suggest using a 3rd order degree polynomial [58]. Obviously, the used parabolic profile can be regarded only as an approximation to these experimental findings. To get a better representation of the velocity profile one may use iteration results of the Cauchy-Riemann equations of higher-order, by conducting a further iteration cycle. This process increases the order of expansion of the u-profile, transforming it into a higher-order polynomial [59]. However, this process increases the order of differentiation of the depth-averaged velocity above U_{xx}, making the numerical solution of the ensuing system of PDEs challenging. The parabolic profile used shall be thus considered as an improvement over using a representation based on the depth-averaged velocity U. Note that the parabolic velocity profile allows backward free surface velocities, e.g., for a horizontal bed the condition is

$$u_s = U - \frac{1}{3}U_{xx}h^2 \leq 0 \Rightarrow U_{xx} \geq \frac{3U}{h^2}. \tag{48}$$

Therefore, in regions with a strong variation of U_x resulting in $U_{xx} > 0$, backward flow velocities may be generated, as in hydraulic jumps, as observed in our numerical simulations.

Overall, the SG equations produces good results, albeit in some test cases, like that in Fig. 8, wave breaking is not strong enough, due to the approximate nature of the model equations. A more accurate representation of wave breaking processes in a depth-averaged framework requires inclusion of the Reynolds stresses in the momentum equations and a turbulence model for closure.

6 Conclusions

In this work, the exact depth-averaged free surface flow equations for flows over uneven beds accounting for the vertical acceleration and differential advection of momentum are presented, thereby generalizing Su and Gardner [10] development. The exact x-momentum equation consists in the leading Saint Venant terms plus corrections terms. These corrections are decomposed into dispersive ones assuming that the horizontal particle velocity equal its depth-averaged value plus other terms including the effect of the non-uniformity of velocity with elevation.

The dispersive corrections based on the depth-averaged velocity produce the terms modeled in the Serre–Green–Naghdi theory, whereas the non-uniform velocity corrections generate high-order non-linear terms. Assuming a parabolic velocity profile identical to that used in Serre–Green–Naghdi theory these high-order terms are quantified for flows over topography, and the ensuing high-order theory is called Su-Gardner theory in recognition to their pioneering work. The high-order terms may equal in magnitude the Serre–Green–Naghdi dispersive corrections at breaking waves, thereby demonstrating that they should be retained in phase resolving models.

The Su-Gardner equations were numerically solved in a number of relevant test cases using a high-resolution finite-volume finite-different solver. The problem of flow over obstacles with breaking waves is relevant in environmental fluid flow modeling and it is an ideal scenario to test the new shallow water approximation pursued here. The test cases included flow adjustment over an isolated ridge in an initially uniform stream, a dam break wave propagation over a tailwater sill and producing a negative surge, the steady flow over a submerged bar with a hydraulic jump at the lee side including a new set of physical experiments, and breaking waves on a slope. It was found in those test cases that the Su-Gardner theory produced solutions close to the Serre–Green–Naghdi theory for non-breaking waves over topography. For breaking waves the Serre–Green–Naghdi theory produced in all cases unrealistic trains of undular waves whereas the new Su-Gardner theory produced shock-like solutions which mimicked wave breaking quite well. The results of this new theory were found to be in conformity with experiments and numerical results from vertically-resolved models in all the tests and for all the waves forming in the computational domain. Neither Serre–Green–Naghdi nor Saint Venant theory were satisfactory.

Wave breaking was automatically mimicked by the Su-Gardner theory through the formation of shock-like solutions thanks to a balancing between the dispersive corrections of the standard Serre–Green–Naghdi theory and the new high-order terms resulting from the non-uniform velocity profile corrections. This balance makes the solution of the Su-Gardner equations at breaking waves similar to that of the Saint Venant equations and very different to that of Serre–Green–Naghdi theory.

The Su-Gardner theory was found to be a natural hybrid between the Serre–Green–Naghdi and Saint Venant shallow water theories, in contrast to actual hybrid models patching Serre–Green–Naghdi and Saint Venant equations in a numerical scheme. In those assembled models some case-dependent empirical parameters need to be calibrated to activate wave breaking. In contrast, in Su-Gardner theory it is the shallow water representation adopted the responsible of wave breaking activation, such that there is not any empirical parameter to calibrate. This new shallow water approximation is therefore a suitable alternative to deal with wave breaking within the Boussinesq-type approximation, and was demonstrated to produce good solutions for flows over obstacles.

Further inclusion of a turbulence model would allow increasing the range of practical cases to be solved, while the model may be extended to two-dimensional flow situations, e.g. undular surge between bridge piers, dam break wave propagation around a building.

Supplementary Information The online version contains supplementary material available at https://doi.org/10.1007/s10652-022-09875-0.

Acknowledgements The work of O. Castro-Orgaz was supported by the Spanish project PID2020-114688RB-I00 and grant María de Maeztu for Centers and Units of Excellence in R&D (Ref. CEX2019-000968-M). FNCC partly was funded by a “Selection of Doctoral Researchers” grant by the Junta-de-Andalucía government, Spain (Ref. DOC_00996), and by MCIN/AEI/10.13039/501100011033 and the NextGeneration EU/PRTR through Juan de la Cierva program (IJC2020-042646-I). The Authors acknowledge the suggestion of Prof. Fréderic Dias of generalizing the Su-Gardner equations to flows over uneven beds.

Author contributions The three authors contributed to all aspects of this research.

Data availability The numerical code developed is available from the corresponding author upon reasonable request. The experimental data is available as supplementary material in the file “Experiments_EFM2022.xls”.

Declarations

Competing interests The authors declare no competing interests.

References

1. Nadiga BT, Margolin LG, Smolarkiewicz PK (1996) Different approximations of shallow fluid flow over an obstacle. Phys Fluids 8(8):2066–2077. https://doi.org/10.1063/1.869009
2. Zhu DZ, Lawrence GA (1998) Non-hydrostatic effects in layered shallow water flows. J Fluid Mech 355:1–16. https://doi.org/10.1017/S0022112097007611
3. Barré de Saint-Venant AJC (1871) Théorie du mouvement non permanent des eaux, avec application aux crues des riviéres et à l’introduction des marées dans leur lit. C R Acad Sci 73:147–154
4. Toro EF (2001) Shock-capturing methods for free-surface shallow flows. Wiley, Singapore
5. Chanson H (2004) The hydraulics of open channel flows: an introduction. Butterworth-Heinemann, Oxford, UK
6. Houghton DD, Kasahara A (1968) Nonlinear shallow fluid flow over an isolated ridge. Commun Pure Appl Math 21:1–23
7. Pratt LJ (1983) A note on nonlinear flow over obstacles. Geophys Astrophys Fluid Dyn 24:63–68. https://doi.org/10.1080/03091928308209058

8. Khan AA, Steffler PM (1996) Vertically averaged and moment equations model for flow over curved beds. J Hydraul Eng 122(1):3–9. https://doi.org/10.1061/(ASCE)0733-9429(1996)122:1(3)
9. Serre F (1953) Contribution à l'étude des écoulements permanents et variables dans les canaux. La Houille Blanche 8(6–7):374−388; 8(12), 830−887
10. Su CH, Gardner CS (1969) KDV equation and generalizations. Part III. Derivation of Korteweg-de Vries equation and Burgers equation. J Math Phys 10(3):536–539
11. Green AE, Naghdi PM (1976) Directed fluid sheets. Proc R Soc Lond A 347:447–473. https://doi.org/10.1098/rspa.1976.0011
12. Green AE, Naghdi PM (1976) A derivation of equations for wave propagation in water of variable depth. J Fluid Mech 78:237–246. https://doi.org/10.1017/S0022112076002425
13. Seabra-Santos FJ, Renouard DP, Temperville AM (1987) Numerical and experimental study of the transformation of a solitary wave over a shelf or isolated obstacle. J Fluid Mech 176:117–134. https://doi.org/10.1017/S0022112087000594
14. Castro-Orgaz O, Cantero-Chinchilla FN (2020) Non-linear shallow water flow modelling over topography with depth-averaged potential equations. Environ Fluid Mech 20(2):261–291. https://doi.org/10.1007/s10652-019-09691-z
15. Biswas TR, Dey S, Sen D (2021) Modeling positive surge propagation in open channels using the Serre–Green–Naghdi equations. Appl Math Model 97:803–820. https://doi.org/10.1016/j.apm.2021.04.028
16. Peregrine DH (1966) Calculations of the development of an undular bore. J Fluid Mech 25(2):321–330. https://doi.org/10.1017/S0022112066001678
17. Peregrine DH (1967) Long waves on a beach. J Fluid Mech 27(5):815–827. https://doi.org/10.1017/S0022112067002605
18. Barthélemy E (2004) Nonlinear shallow water theories for coastal waters. Surv Geophys 25(3):315–337. https://doi.org/10.1007/s10712-003-1281-7
19. Naghdi PM, Vongsarnpigoon L (1986) The downstream flow beyond an obstacle. J Fluid Mech 162:223–236. https://doi.org/10.1017/S0022112086002021
20. Teles da Silva AF, Peregrine DH (1992) Wave-breaking due to moving submerged obstacles. Breaking Waves, IUTAM Symposium Sydney/Australia 1991,Springer, Berlin, pp 333−340. https://doi.org/10.1007/978-3-642-84847-6_38
21. Farmer DM, Denton RA (1985) Hydraulic control of flow over the sill in Observatory inlet. J Geophys Res Oceans 90(C5):9015–9068. https://doi.org/10.1029/JC090iC05p09051
22. Denton RA (1987) Locating and identifying hydraulic controls for layered flow through an obstruction. J Hydraul Res 25(3):281–299. https://doi.org/10.1080/00221688709499271
23. Ai C, Ma Y, Ding W, Xie Z, Dong G (2021) An efficient three-dimensional non-hydrostatic model for undular bores in open channels. Phys Fluids 33:127111. https://doi.org/10.1063/5.0073241
24. Ai C, Ma Y, Ding W, Xie Z, Dong G (2022) Three-dimensional non-hydrostatic model for dam-break flows. Phys Fluids 34:022105. https://doi.org/10.1063/5.0081094
25. Castro-Orgaz O, Chanson H (2020) Undular and broken surges in dam-break flows: A review of wave breaking strategies in a Boussinesq-type framework. Environ Fluid Mech 20(6):1383–1416. https://doi.org/10.1007/s10652-020-09749-3
26. Castro-Orgaz O, Chanson H (2017) Ritter's dry-bed dam-break flows: positive and negative wave dynamics. Environ Fluid Mech 17(4):665–694. https://doi.org/10.1007/s10652-017-9512-5
27. Tonelli M, Petti M (2009) Hybrid finite volume—Finite difference scheme for 2DH improved Boussinesq equations. Coastal Eng 56(5–6):609–620. https://doi.org/10.1016/j.coastaleng.2009.01.001
28. Kazolea M, Delis AI, Synolakis CE (2014) Numerical treatment of wave breaking on unstructured finite volume approximations for extended Boussinesq-type equations. J Comput Phys 271:281–305. https://doi.org/10.1016/j.jcp.2014.01.030
29. Kazolea M, Ricchiuto M (2018) On wave breaking for Boussinesq-type models. Ocean Model 123:16–39. https://doi.org/10.1016/j.ocemod.2018.01.003
30. Rouse H (1938) Fluid mechanics for hydraulic engineers. McGraw-Hill, New York
31. Vallentine HR (1969) Applied hydrodynamics. Butterworths, London
32. Castro-Orgaz O, Hager WH (2017) Non-hydrostatic free surface flows. Advances in geophysical and environmental mechanics and mathematics. Springer, Berlin. https://doi.org/10.1007/978-3-319-47971-2
33. Shimozono T, Ikewaza H, Sato S (2017) Non-hydrostatic modeling of coastal levee overflows. Coastal Dyn 2017:1606–1615
34. Carter JD, Cienfuegos R (2011) The kinematics and stability of solitary and cnoidal wave solutions of the Serre equations. Eur J Mech B Fluids 30(3):259–268. https://doi.org/10.1016/j.euromechflu.2010.12.002
35. Castro-Orgaz O, Hager WH (2014) 1D modelling of curvilinear free surface flow: generalized Matthew theory. J Hydraul Res 52(1):14–23. https://doi.org/10.1080/00221686.2013.834853
36. Tuck EO (1992) Can shallow-water theory describe breaking? Breaking Waves, IUTAM Symposium Sydney/Australia 1991. Springer, Berlin, pp 341−345. https://doi.org/10.1007/978-3-642-84847-6_39

37. Peregrine DH, Cokelet ED, Mciver P (1980) The fluid mechanics of waves approaching breaking. Coast Eng Proc 17:31. https://doi.org/10.1061/9780872622647.032
38. Brocchini M, Dodd N (2008) Nonlinear shallow water equation modeling for coastal engineering. J Waterw Port Coast Ocean Eng 134(2):104–120. https://doi.org/10.1061/(ASCE)0733-950X(2008)134:2(104)
39. Cienfuegos R, Barthélemy E, Bonneton P (2006) A fourth-order compact finite volume scheme for fully nonlinear and weakly dispersive Boussinesq-type equations. Part I: Model development and analysis. Int J Num Meth Fluids 51(11):1217–1253. https://doi.org/10.1002/fld.1141
40. Gottlieb S, Shu CW, Tadmor E (2001) Strong stability-preserving high-order time discretization methods. SIAM Rev 43(1):89–112. https://doi.org/10.1137/S003614450036757X
41. Erduran KS, Ilic S, Kutija V (2005) Hybrid finite-volume finite-difference scheme for the solution of Boussinesq equations. Int J Numer Methods Fluids 49(11):1213–1232. https://doi.org/10.1002/fld.1021
42. Abramowitz M, Stegun IA (1972) Handbook of mathematical functions with formulas, graphs, and mathematical tables, 10th edn. Wiley, New York
43. Long RR (1954) Some aspects of the flow of stratified fluids II, experiments with a two-fluid system. Tellus 5:42–58. https://doi.org/10.1111/j.2153-3490.1954.tb01100.x
44. Long RR (1970) Blocking effects in flow over obstacles. Tellus 22:471–480. https://doi.org/10.3402/tellusa.v22i5.10241
45. Sivakumaran NS, Tingsanchali T, Hosking RJ (1983) Steady shallow flow over curved beds. J Fluid Mech 128:469–487. https://doi.org/10.1017/S0022112083000567
46. Ozmen-Cagatay H, Kocaman S (2011) Dam-break flow in the presence of obstacle: experiment and CFD simulation. Eng Appl Comput Fluid Mech 5(4):541–552. https://doi.org/10.1080/19942060.2011.11015393
47. Soares Frazão S, Zech Y (2007) Experimental study of dam-break flow against an isolated obstacle. J Hydraul Res 45:27–36. https://doi.org/10.1080/00221686.2007.9521830
48. Mignot E, Cienfuegos R (2009) On the application of a Boussinesq model to river flows including shocks. Coast Eng 56(1):23–31. https://doi.org/10.1016/j.coastaleng.2008.06.007
49. Chanson H (1996) Free-surface flows with near-critical flow conditions. Can J Civ Eng 23(6):1272–1284. https://doi.org/10.1139/l96-936
50. Chanson H, Montes JS (1995) Characteristics of undular hydraulic jumps: Experimental apparatus and flow patterns. J Hydraulic Eng 121(2):129–144; 123(2):161–164. https://doi.org/10.1061/(ASCE)0733-9429(1995)121:2(129)
51. Castro-Orgaz O (2010) Weakly undular hydraulic jump: effects of friction. J Hydraul Res 48(4):453–465. https://doi.org/10.1080/00221686.2010.491646
52. Wang H, Murzyn F, Chanson H (2014) Total pressure fluctuations and two-phase flow turbulence in hydraulic jumps. Exp Fluids 55:1847. https://doi.org/10.1007/s00348-014-1847-9
53. Synolakis CE (1986) The runup of long waves. Ph.D. Thesis, California Institute of Technology, California
54. Barthelemy X, Banner ML, Peirson WL, Fedele F, Allis M, Dias F (2018) On a unified breaking onset threshold for gravity waves in deep and intermediate depth water. J Fluid Mech 841:463–488
55. Rajaratnam N (1965) The hydraulic jump as a wall jet. J Hydr Div ASCE 91(HY5):107–132
56. Chanson H, Brattberg T (2000) Experimental study of the air-water shear flow in a hydraulic jump. Int J Multiph Flow 26(4):583–607. https://doi.org/10.1016/S0301-9322(99)00016-6
57. Wang H, Chanson H (2015) Air entrainment and turbulent fluctuations in hydraulic jumps. Urban Water J 12(6):502–518. https://doi.org/10.1080/1573062X.2013.847464
58. Madsen PA, Svendsen IA (1983) Turbulent bores and hydraulic jumps. J Fluid Mech 129:1–25
59. Castro-Orgaz O, Cantero-Chinchilla FN, Hager WH (2022) High-order shallow water expansions in free surface flows: application to steady overflow processes. Ocean Eng 250:110717

Authors and Affiliations

Oscar Castro-Orgaz[1] · Francisco N. Cantero-Chinchilla[1] · Hubert Chanson[2]

Francisco N. Cantero-Chinchilla
z12cachf@uco.es

Hubert Chanson
h.chanson@uq.edu.au

[1] Hydraulic Engineering Area, University of Cordoba, Rabanales Campus, Leonardo da Vinci Building, 14071 Córdoba, Spain

[2] School of Civil Engineering, The University of Queensland, Brisbane, QLD 4072, Australia